



# HyspIRI High-Temperature Saturation Study

*V. Realmuto*

*S. Hook*

*M. Foote*

*Jet Propulsion Laboratory*

*I. Csiszar*

*NOAA/NESDIS Center for Satellite Applications and Research*

*Camp Springs, MD*

*P. Dennison*

*University of Utah*

*Salt Lake City, UT*

*L. Giglio*

*University of Maryland*

*College Park, MD*

*M. Ramsey*

*University of Pittsburgh*

*Pittsburgh, PA*

*R.G. Vaughan*

*USGS Astrogeology Science Center*

*Flagstaff, AZ*

*M. Wooster*

*King's College London*

*London*

*R. Wright*

*University of Hawaii at Manoa*

*Honolulu, HI*

**National Aeronautics and  
Space Administration**

**Jet Propulsion Laboratory**

**California Institute of Technology**

**Pasadena, California**

This research was carried out at the Jet Propulsion Laboratory, California Institute of Technology, under a contract with the National Aeronautics and Space Administration.

Reference herein to any specific commercial product, process, or service by trade name, trademark, manufacturer, or otherwise, does not constitute or imply its endorsement by the United States Government or the Jet Propulsion Laboratory, California Institute of Technology.

© 2011. All rights reserved.

## Contents

1	SUMMARY .....	1-1
2	INTRODUCTION .....	2-1
2.1	Heritage Instruments .....	2-4
3	THE REMOTE ESTIMATION OF TEMPERATURE .....	3-1
3.1	The MODIS Fire Detection Algorithm .....	3-4
3.2	The MODVOLC Algorithm .....	3-6
3.3	Sub-Pixel Temperature Models .....	3-8
3.4	Minimized Multi-Component Modeling .....	3-9
3.5	Spectral Endmember Mapping .....	3-10
3.6	Fire Radiant Power .....	3-12
4	CASE STUDIES .....	4-1
4.1	Published Studies .....	4-1
4.2	Team Studies .....	4-2
4.2.1	AMS Survey of Southern California Wildfires .....	4-2
4.2.2	AGEMA Camera Data for Sharpsand Creek Fire .....	4-10
4.2.3	AVIRIS Survey of the Indians Fire .....	4-13
4.2.4	ASTER Surveys of Klyuchevskoy and Kilauea Volcanoes .....	4-15
4.2.5	Hyperion Surveys of Nyamuragira and Eyjafjallajökull Volcanoes .....	4-18
5	CONCLUSION .....	5-1
6	SELECTED BIBLIOGRAPHY .....	6-1

## **1 Summary**

---

As part of the precursor activities for the HyspIRI mission, a small team was assembled to determine the optimum saturation level for the mid-infrared (4- $\mu\text{m}$ ) channel, which is dedicated to the measurement of hot targets. Examples of hot targets include wildland fires and active lava flows. This determination took into account both the temperature expected for the natural phenomena and the expected performance of the mid-infrared channel as well as its overlap with the other channels in the thermal infrared (7.5–12  $\mu\text{m}$ ) designed to measure the temperature of lower temperature targets. Based on this work, the hot target saturation group recommends a saturation temperature of 1200 K for the mid-infrared channel. The saturation temperature of 1200 K represents a good compromise between the prevention of saturation and sensitivity to ambient temperature.

## 2 Introduction

---

In 2004, the National Aeronautics and Space Administration (NASA), the National Oceanic and Atmospheric Administration (NOAA), and the U.S. Geological Survey (USGS) requested that the National Research Council (NRC) identify and prioritize the satellite platforms and associated observational capabilities that should be launched and operated over the next decade for Earth observation. In addition to providing information for the purpose of addressing scientific questions, the committee identified the need to ensure that the measurements helped benefit society and provide policymakers with the necessary information to make informed decisions on future policies affecting the Earth.

The resulting NRC study *Earth Science and Applications from Space: National Imperatives for the Next Decade and Beyond*, also known as the Earth Science Decadal Survey (NRC 2007), recommended launching 15 missions in three time phases. These three time phases are referred to as Tier 1, Tier 2, and Tier 3. The Hyperspectral Infrared Imager (HyspIRI) mission is one of the Tier 2 missions recommended for launch in the 2013–2016 timeframe. The mission will advance our scientific understanding of how the Earth is changing as well as provide valuable societal benefit, particularly in understanding and tracking dynamic events such as volcanoes and wildfires.

The HyspIRI mission includes two instruments: a Visible-Shortwave Infrared (VSWIR) imaging spectrometer and a Thermal Infrared (TIR) multispectral scanner. The VSWIR instrument will measure the radiance in 212 channels between 0.38 and 2.5 micrometers ( $\mu\text{m}$ ) at a spatial resolution of 60 m. The VSWIR ground track will have a swath width of 145 km and revisit time of 19 days at the equator. The TIR instrument will measure the radiance in 8 channels between 4 and 12  $\mu\text{m}$  at a spatial resolution of 60 m. The TIR ground track will have a swath width of 600 km and revisit time of 5 days at the equator.

The current specifications for the HyspIRI TIR channels, with the exception of a proposed channel centered at 7.5  $\mu\text{m}$ , are shown in Figure 1. These channels include a mid-infrared (MIR) channel, positioned near 4  $\mu\text{m}$ , for investigations of high-temperature phenomena such as wildland fires and active lava flows and domes. The channels are superimposed on the radiance spectra of blackbodies at temperatures of 300, 500, and 700 K (Fig. 1). We present a detailed discussion of the fundamentals of blackbody radiation in Section 3; Figure 1 is an explanation for the positions of the HyspIRI TIR channels. The channels between 8 and 12  $\mu\text{m}$  are well positioned to measure the radiance of a blackbody at 300 K (Fig. 1), the average temperature of the Earth’s surface. The HyspIRI channels between 8 and 12  $\mu\text{m}$  are designed to saturate at temperatures near 500 K, the approximate cross-over temperature at which the blackbody radiance at 4 and 8  $\mu\text{m}$  is roughly equivalent (Fig. 1). The radiance of a blackbody at 700 K peaks near the center of the proposed 4- $\mu\text{m}$  channel.

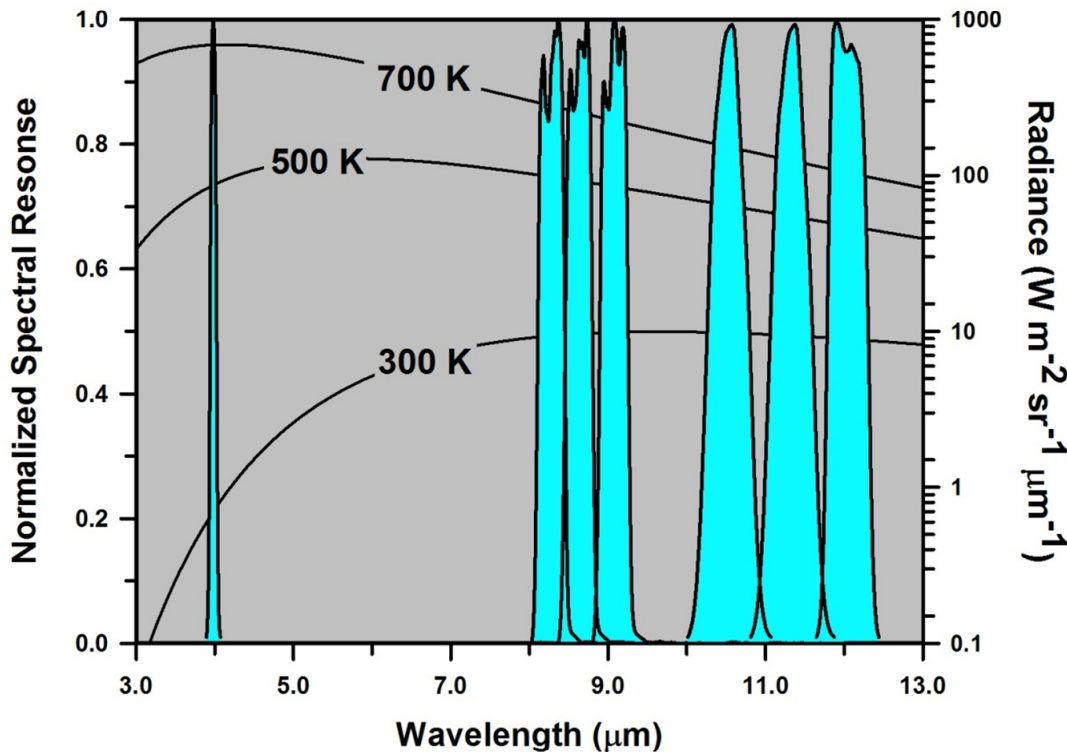


**Figure 1. Normalized Spectral Response of HyspIRI Channels in the Mid (4  $\mu\text{m}$ ) and Thermal Infrared (8 – 12  $\mu\text{m}$ ). The Spectral Response Functions (shown in blue) are Superimposed on Blackbody Radiance Spectra for Temperatures of 300, 500, and 700 K.**

The importance of the 4- $\mu\text{m}$  channel to the HyspIRI science objectives is evident in the number of science questions that require high-temperature measurements. The science questions are listed below; the information in brackets denotes the relevant pages of the NRC Decadal Survey.

**TQ1:** How can we help predict and mitigate earthquake and volcanic hazards through detection of transient thermal phenomena?

- What do changes in the rate of lava effusion tell us about the maximum lengths that lava flows can attain and the likely duration of lava flow-forming eruptions? [DS 226]

**TQ2:** What is the impact of global biomass burning on the terrestrial biosphere and atmosphere, and how is this impact changing over time?

- How are global fire regimes changing in response to, and driven by, changing climate, vegetation, and land use practices? [DS 198]
- Is regional and local scale fire frequency changing? [DS 196]
- What is the role of fire in global biogeochemical cycling, particularly trace gas emissions? [DS 195]
- Are there regional feedbacks between fire and climate change?

**CQ2:** How are fires and vegetation composition coupled?

- How do the timing, temperature, and frequency of fires affect long-term ecosystem health?
- How do vegetation composition and fire temperature impact trace gas emissions?
- How do fires in coastal biomes affect terrestrial biogeochemical fluxes into estuarine and coastal waters and what is the subsequent biological response? **[DS 198]**
- What are the feedbacks between fire temperature and frequency and vegetation composition and recovery?
- How does vegetation composition influence wildfire severity?

**CQ3:** Do volcanoes signal impending eruptions through changes in the temperature of the ground, rates of gas and aerosol emission, temperature and composition of crater lakes, or health and extent of vegetation cover?

- What do comparisons of thermal flux and SO<sub>2</sub> emission rates tell us about the volcanic mass fluxes and the dynamics of magma ascent? **[DS 227; 230]**
- Can measurements of the rate at which lava flows cool allow us to improve forecasts of lava flow hazards? **[DS 50; 226]**
- Do changes in the health and extent of vegetation cover indicate changes in the release of heat and gas from crater regions? **[DS 230; 231]**

The goal of this study was to identify an optimum temperature setting that prevents saturation of the 4- $\mu\text{m}$  measurements over targets of interest while providing useful overlap with measurements made with the remaining TIR channels (Fig. 1). The TIR channels will saturate between 450 and 500 K, leading us to evaluate the impact of the 4- $\mu\text{m}$  saturation temperature on the sensitivity of the MIR channel to scene temperatures less than 500 K. One metric for sensitivity is the noise-equivalent temperature difference (NE $\Delta$ T), which is the smallest difference in temperature that can be measured in the presence of noise.

Figure 2 shows the anticipated NE $\Delta$ T as a function of saturation and scene temperature. For scene temperatures  $\geq 500$  K the saturation temperature does not have much effect on the NE $\Delta$ T. The sensitivity decreases (i.e., NE $\Delta$ T increases) with decreasing scene temperature, regardless of the saturation temperature. For a given scene temperature, the sensitivity will decrease with an increase in saturation temperature. At a scene temperature of 340 K, for example, saturation temperature settings of 800 and 1400 K will result in NE $\Delta$ T values of 1.5 and 7.0 K, respectively (Fig. 2).

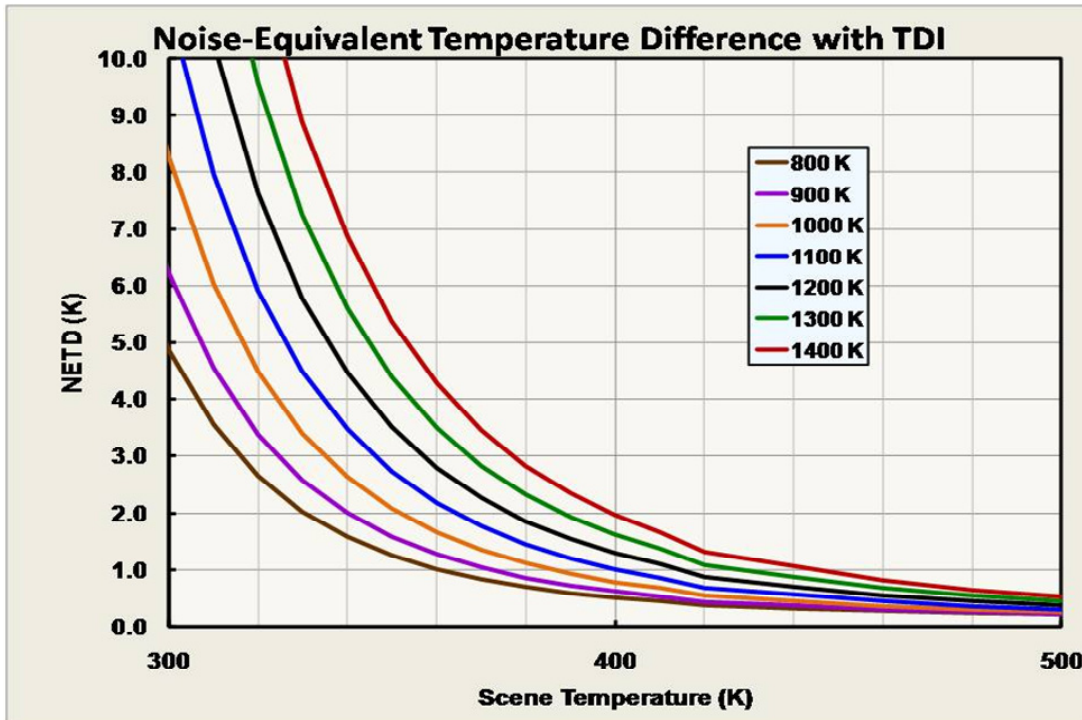


**Figure 2.** Simulated sensitivity of the HyspIRI 4- $\mu$ m Channel to scene temperatures between 300 and 500 K. The sensitivity is expressed as Noise Equivalent Temperature Difference (NE $\Delta$ T). For a scene temperature of 340 K a saturation temperature of 800 K results in an NE $\Delta$ T of 1.5 K, while a saturation temperature of 1400 K results in an NE $\Delta$ T of 7 K.

## 2.1 Heritage Instruments

Table 1 lists current and recent satellite instruments equipped with MIR channels positioned near 4  $\mu$ m. The data from all of these instruments have been applied to studies of high-temperature phenomena (cf. Selected Bibliography), but only MODIS and the Hot Spot Recognition System (HSRS) on board the Bi-spectral Infrared Detection (BIRD) satellite, designed and operated by DLR, were designed specifically to measure high temperatures.

The column highlighted in yellow lists the spatial resolution of the heritage instruments (Table 1). The 60-m spatial resolution of HyspIRI represents a significant improvement over that of the heritage instruments. For example, one HSRS pixel, with a resolution of 370 meters, would enclose 36 HyspIRI pixels.

**Table 1. HyspIRI Heritage: Imaging Instruments with MIR Channels**

Instrument	Central Wavelength	Spatial Resolution (at nadir)	Temporal Coverage (daytime)	Saturation Temperature
AVHRR	3.7 $\mu$ m	1.1 km	Daily (NOAA 18 + 19)	~ 321.5 K
VIRS (TRMM)	3.75 $\mu$ m	2.4 km	2 day revisit	321K
ATSR/AATSR	3.7 $\mu$ m	1 km /1.5 x 2 km	3 day revisit	311 K
MODIS	3.95 $\mu$ m	1 km	Daily (Terra + Aqua)	478 K /506 K (Ch. 21); 330 K (Ch. 22)
GOES Imager	3.9 $\mu$ m	2.3 x 4 km	3 hr/15-30 min	335 K
SEVIRI (MSG)	3.9 $\mu$ m	3 km	15 min	335 K
HSRS (BIRD)	3.4 – 4.2 $\mu$ m	370 m	Targeted	600 K

The data acquired with MODIS Channels 21 and 22 provide a real-world example of the relationship between saturation temperature and sensitivity. The channels have the same spectral response, but Channel 21, the so-called “Fire Channel,” was designed with a higher saturation temperature than Channel 22 (500 vs. 330 K). As a consequence of the higher saturation temperature, Channel 21 is less sensitive to scene temperatures ~300 K than Channel 22 (NE $\Delta$ T of 0.8 K for Ch. 21 vs. 0.03 K for Ch. 22). As noted by Gao et al. (2007), the Channel 21 data have proven to be too noisy for use in an operational estimation of fire temperature. In addition, the use of Channel 21 data in the operational MODIS fire detection algorithm is limited to cases when the Channel 22 data are saturated.

To re-evaluate the saturation temperature for MODIS Channel 21, Gao et al. derived temperature estimates for pixels flagged by the MODIS fire detection algorithm from over 40 sets of Channel 21 data acquired by MODIS-Terra and MODIS-Aqua. Figure 3 shows histograms of these temperature estimates. The cumulative histogram (Fig. 3[b]) indicates that 90% of the temperatures were less than 350 K. Given that the great majority of temperature estimates fell within the range of low Channel 21 sensitivity, Gao et al. recommended a saturation temperature  $\leq$  450 K for any future instruments with 4- $\mu$ m channels with a spatial resolution of 1 km.

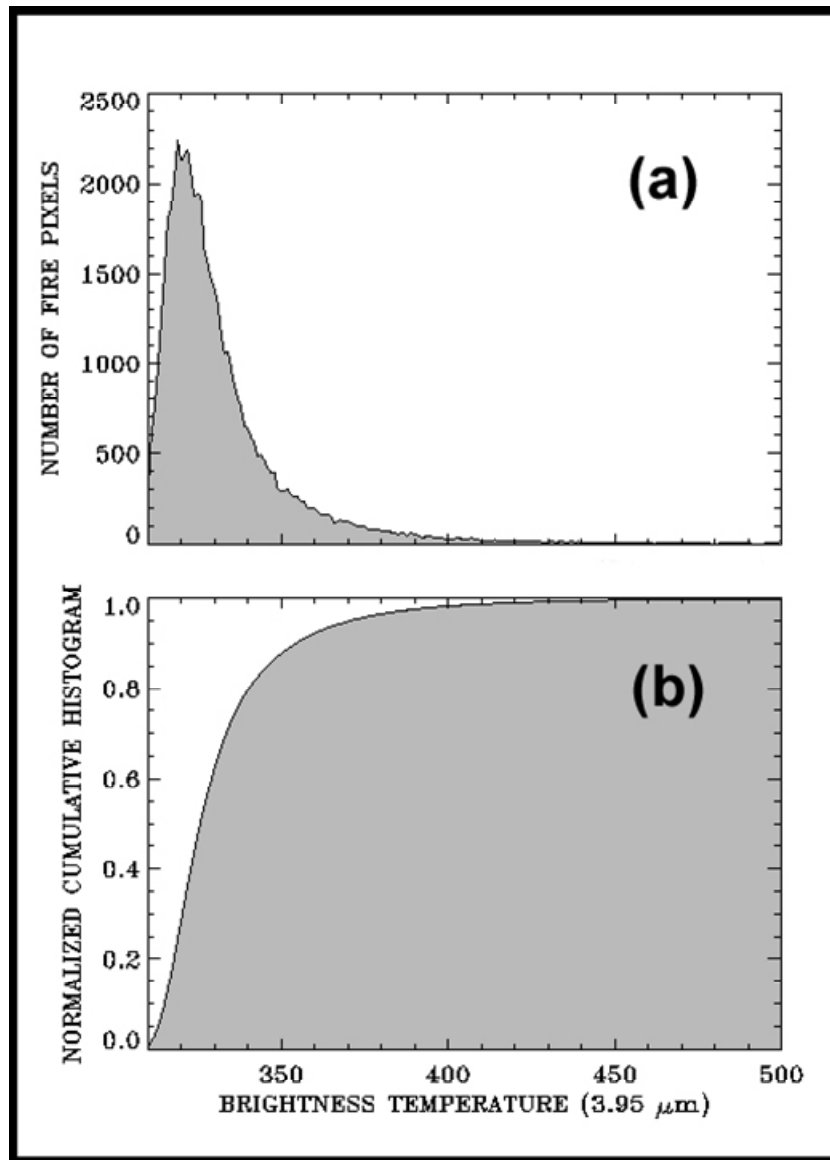


**Figure 3. Fire pixels histograms compiled by Gao et al. [2007].**  
(a) Relative frequency plot; (b) cumulative probability plot.  
Note that 90% of the 4- $\mu\text{m}$  temperatures were  $\leq 350$  K.

The recommendation of Gao et al. (2007) is the result of a probability-based approach, in which the saturation temperature was set to the highest scene temperature that we are likely to encounter. However, many of the high-temperature phenomena identified in the HyspIRI science questions are the result of unique events, which, by definition, have low probabilities of occurrence. In Figure 4 we show rank-order plots of brightness temperatures for three volcanoes—Kilauea, Etna, and Nyamuragira (Figs. 4[a], [b], and [c], respectively)—accumulated over the period 2000–2009. We see that all three volcanoes produced temperatures in excess of 478 K, the saturation temperature of MODIS-Terra Channel 21 (Xiong et al. 2009), while Etna and Nyamuragira produced temperatures in excess of 506 K, the saturation temperature of MODIS-Aqua Channel 21. In all three cases, a saturation temperature of 450 K would preclude measurements of such high-temperature events.

For another argument against a 4- $\mu\text{m}$  saturation temperature of 450 K, we recall that the HyspIRI TIR channels centered between 8 and 13  $\mu\text{m}$  will have saturation temperatures of 500 K. Therefore, in the case of HyspIRI, a 4- $\mu\text{m}$  channel with a saturation temperature less than 500 K will provide no additional information about high-temperature phenomena relative to the TIR channels.

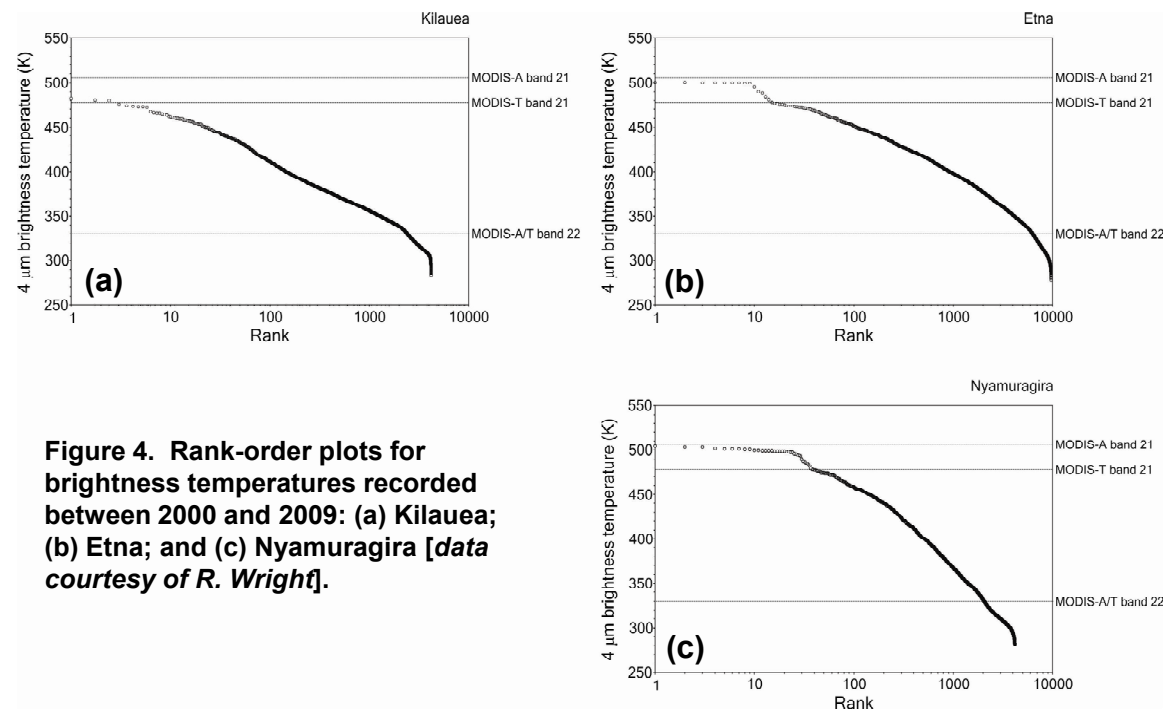


**Figure 4. Rank-order plots for brightness temperatures recorded between 2000 and 2009: (a) Kilauea; (b) Etna; and (c) Nyamuragira [data courtesy of R. Wright].**

### 3 The Remote Estimation of Temperature

---

In the following sections, we will present airborne and satellite observations to support our recommendation for saturation temperature. We note that neither HyspIRI nor any of the heritage instruments from Table 1 make direct measurements of surface temperature. The instruments measure scene radiance, and we must derive estimates of temperature from these radiance measurements. The 4- $\mu\text{m}$  channel will be designed for a maximum level of radiance, and the saturation temperature will correspond to the maximum radiance.

We do not have radiance data at the spatial resolution and spectral response of HyspIRI, so we must work with radiance measured at spatial resolutions and spectral responses different from the notional HyspIRI parameters. As we demonstrate below, temperature estimates depend strongly on the spatial resolution and spectral response of the corresponding radiance measurements. To discuss these dependences, we first present a brief review of the theory and practice of remote estimates of temperature.

The relationship between the temperature of a surface and spectral radiance emitted from the surface is described by the Planck blackbody law:

$$B_\lambda(T) = \frac{C_1}{\pi\lambda^5 \left[ \exp\left(\frac{C_2}{\lambda T}\right) - 1 \right]},$$

where  $T$  and  $\lambda$  represent temperature in Kelvins (K) and wavelength in micrometers ( $\mu\text{m}$ ), respectively. The resulting units of radiance are Watts per unit area, solid angle, or steradian, and wavelength ( $\text{W m}^{-2} \text{ sr}^{-1} \mu\text{m}^{-1}$ ).  $C_1$  and  $C_2$  are the first and second radiation constants, defined as

$$C_1 = 3.74151 \times 10^8 \text{ W m}^2 \mu\text{m}^4 \text{ (or } 3.74151 \times 10^{-16} \text{ W m}^2\text{)} \text{ and}$$
$$C_2 = 1.43879 \times 10^4 \mu\text{m K} \text{ (or } 1.43879 \times 10^{-2} \text{ m K}\text{)}.$$

The Planck Law describes an idealized perfect radiator. The relationship between the radiance of a real-world surface and that of a blackbody is given by:

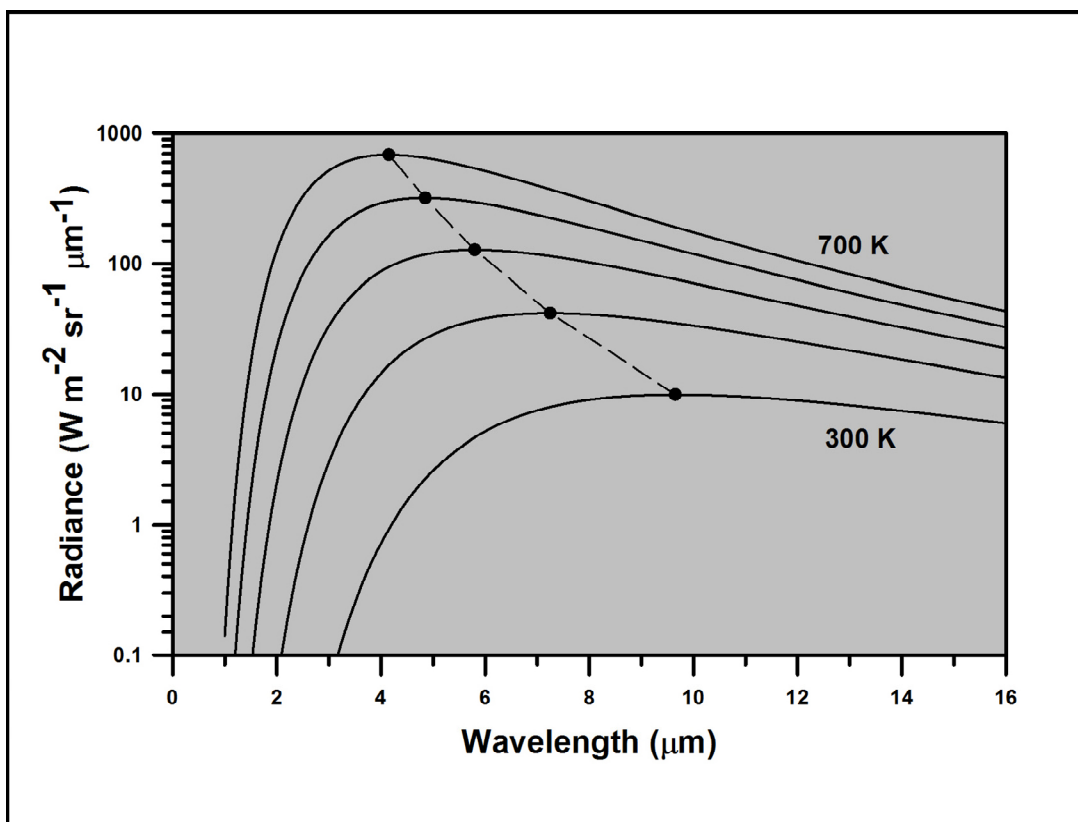
$$L(\lambda, T) = \varepsilon(\lambda)B(\lambda, T),$$

where  $\varepsilon(\lambda)$  represents the spectral emissivity of the surface. By definition, the emissivity of a blackbody is constant and equal to 1.0. A graybody is an idealized radiator with a constant emissivity less than 1.0. The emissivity of most real-world surfaces varies with wavelength, and emissivity spectra are used to identify materials and estimate material properties.

Given a radiance spectrum, we can invert the Planck law to derive an estimate of temperature. If we assume that the surface is a blackbody, then the resulting temperature estimate is known as a brightness temperature. We may also assign an emissivity spectrum to the surface before deriving temperature estimates. In either situation, we will obtain temperature estimates that vary with wavelength if our knowledge of emissivity is not perfect.

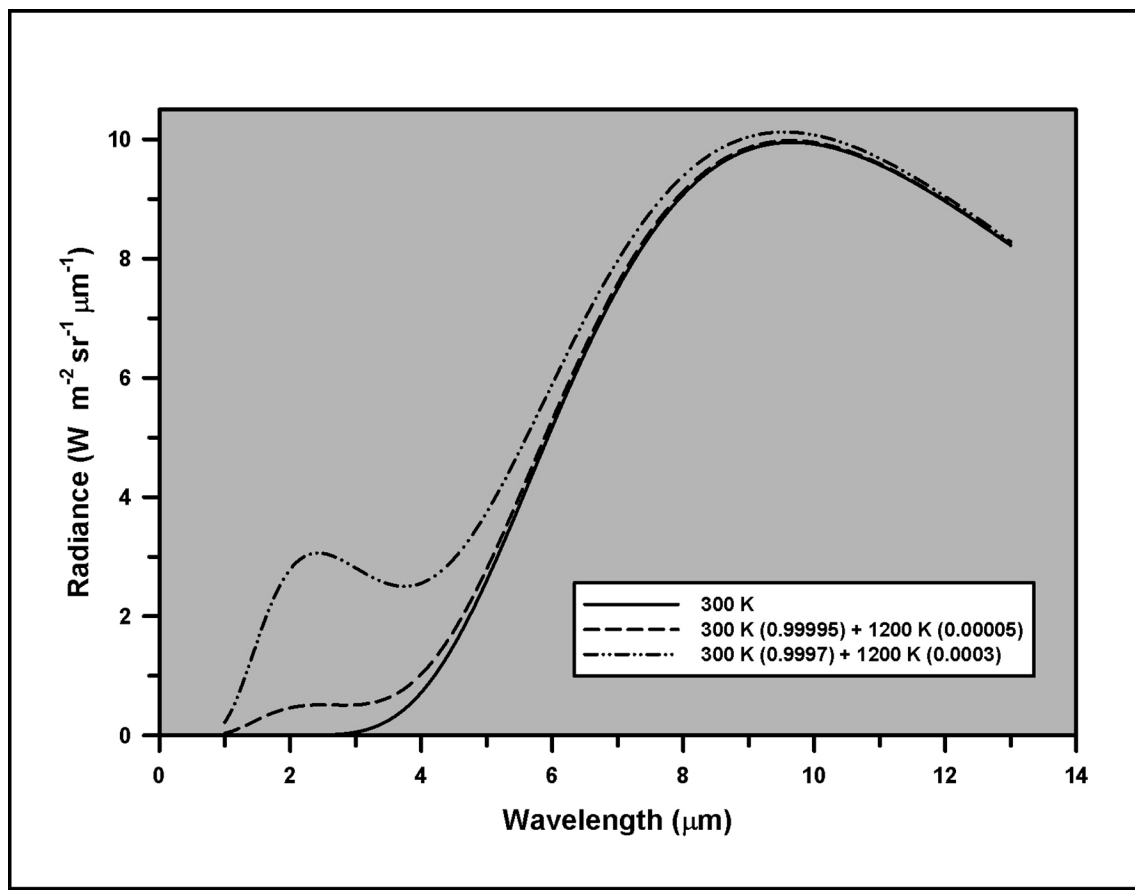
In practice, the estimation of temperature from remote sensing measurement is more complicated than the theory discussed previously. For the purposes of this study, the most important consideration is the non-uniform distribution of surface temperatures within the instantaneous field of view of a sensor. Here we discuss this sub-pixel mixing of temperatures in greater detail.

Figure 5 illustrates the radiance spectra for surface temperatures ranging from 300 to 700 K. We note that the peak radiance, signified by the solid circles (Fig. 5), shifts to shorter wavelengths as the temperature increases. Wien's Displacement Law describes the relation between the wavelength of the peak radiance and temperature as  $\lambda_{max} = b/T$ , where  $b \sim 3 \times 10^{-3} \text{ m}\cdot\text{K}$ . The radiance at 300 K peaks near 10  $\mu\text{m}$  (Fig. 5), the approximate center of the wavelength range covered by the HyspIRI TIR channels (8–12  $\mu\text{m}$ ). The radiance at 700 K peaks near 4  $\mu\text{m}$ , highlighting the need for a 4- $\mu\text{m}$  channel to study high-temperature phenomena.



**Figure 5. Illustration of Wien's Displacement Law for surface temperatures between 300 – 700 K. The solid circles indicate the peak radiance of each spectrum.**

Figure 6 illustrates the radiance spectra resulting from sub-pixel mixing of two temperature components (Wright et al. 2002). The solid line represents the spectrum of a surface at a uniform temperature of 300 K. The dashed line represents the spectrum resulting from a mixture of components at 300 and 1200 K temperatures, with the hot component occupying 0.005% of the surface area. In accordance with Wien's Displacement Law (Fig. 5), the presence of this hot component increases radiance at wavelengths  $< 6.0 \mu\text{m}$ , relative to the isothermal spectrum, and has less effect on the radiance at longer wavelengths (Fig. 6). The broken line represents the spectrum resulting from an increase in the size of the 1200 K component to 0.03% of the surface area. The presence of this larger hot component increases the radiance at all wavelengths, relative to the isothermal spectrum, with the greatest increase occurring at the shorter wavelengths. Accordingly, the difference between brightness temperatures calculated at short and long wavelengths, such as 4 and 11  $\mu\text{m}$ , will increase with increases in the area and/or temperature of the hot fraction. The detection of such variation from isothermal radiance is the foundation of the operational MODIS fire and MODVOLC hot-spot detection algorithms, which we discuss in the next section.



**Figure 6. Compound radiance spectra resulting from sub-pixel mixture of two temperature components [after Wright et al., 2002].**

### 3.1 The MODIS Fire Detection Algorithm

The MODIS project generates fire detection maps in Level 2 (MOD14/MYD14) and Level 3 daily (MOD14A1/MYD14A1) and 8-day (MOD14A2/MYD14A2) formats. The maps show the locations of pixels classified as “active” fire. The fire detection algorithm (Justice et al. 2002; Kaufman et al. 2003) uses brightness temperatures derived from radiance measurements at 4 and 11  $\mu\text{m}$ , denoted by  $T_4$  and  $T_{11}$ , respectively.  $T_4$  is derived from Channel 22 whenever possible, as this channel has smaller quantization errors (0.03 vs. 0.8 K for a surface temperature of 300 K). When Channel 22 saturates, or these data are missing,  $T_4$  is derived from Channel 21.  $T_{11}$  is derived from Channel 31, which was designed to saturate at 400 and 340 K for MODIS-Terra and MODIS-Aqua, respectively.

The fire detection algorithm operates in two modes. The absolute, or spectral, mode is based on pre-defined thresholds on  $T_4$  and the difference between  $T_4$  and  $T_{11}$  ( $T_4 - T_{11}$ ). If the derived values fall below these thresholds, the detection algorithm switches to the relative, or context, mode in which the values of  $T_4$  and ( $T_4 - T_{11}$ ) at a pixel are compared to the values from surrounding pixels. The region of interest surrounding the pixel under consideration increases in area until a pre-defined number of fire-free pixels are identified.

The metrics for the accuracy of the detection include probabilities of detection and commission/omission error rates. These metrics are based on ground truth data at the scale of the MODIS footprint and ASTER data acquired coincidently with MODIS-Terra data (Csiszar et al. 2006; Morisette et al. 2005a, 2005b). Figure 7 shows an ASTER scene, acquired over a fire in Siberia, superimposed with the corresponding output of the MODIS fire detection algorithm. Such comparisons between MODIS and ASTER data products have revealed that a MODIS pixel must enclose 45 to 60 contiguous ASTER fire pixels in order to have a 50% probability of being classified as fire. Similarly, a MODIS pixel must enclose at least 50 contiguous ASTER fire pixels to achieve omission, or false negative, probabilities below 40%. The probability of commission errors, or false positives, is typically  $<0.1\%$ , due to the fact that MODIS does not, in general, detect fires that are not detected in the corresponding ASTER data.

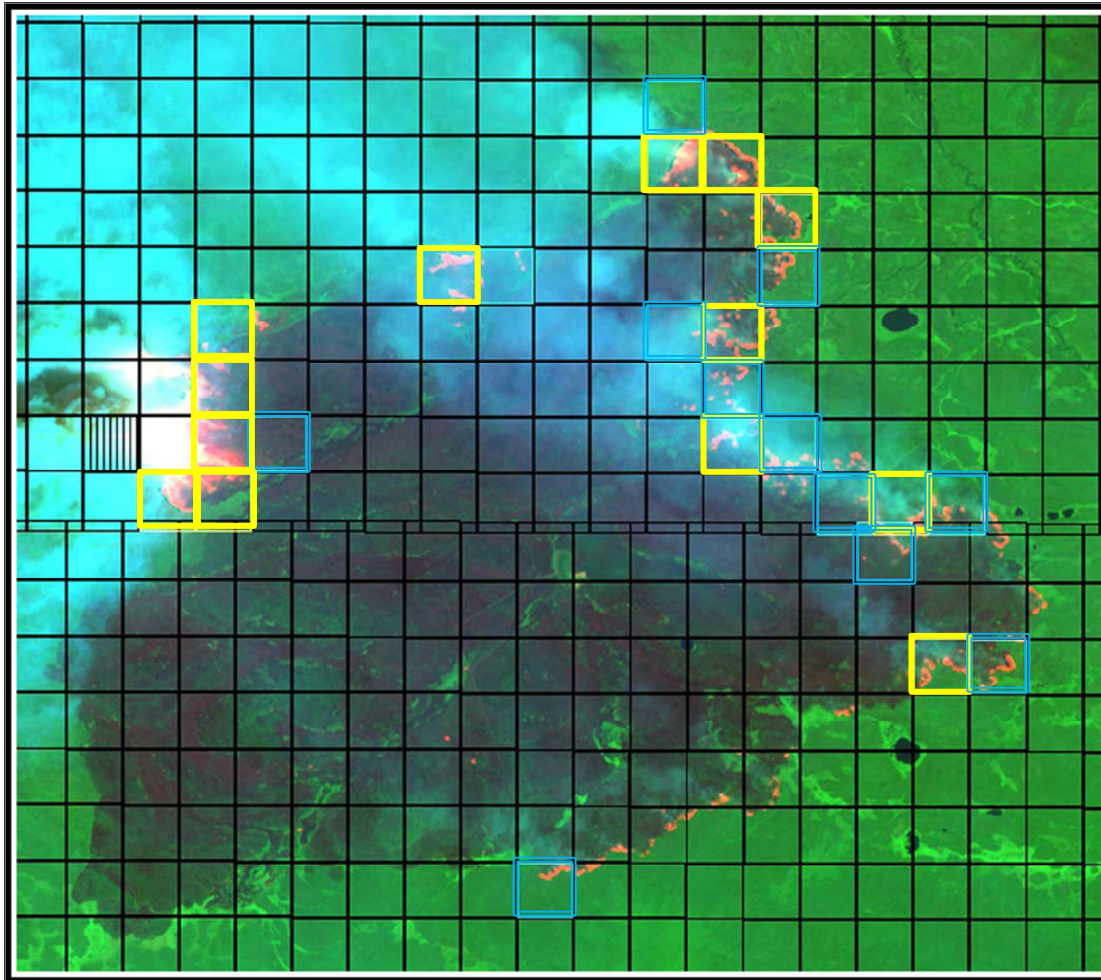


**Figure 7. MODIS 1-km grid superimposed over ASTER color-composite scene depicting a fire in Siberia (62.57 °N, 125.72 °E). Yellow and blue grid cells correspond to MODIS fire pixels identified with high and nominal confidence, respectively [Csiszar et al., 2006].**

The potential contribution of HyspIRI to fire detection programs is illustrated in Figure 8, which is a plot of the theoretical limit, or threshold, of detection for the MODIS fire algorithm as a function of the size and temperature of a fire (Giglio et al. 1999; Csiszar et al. 2006). Fires with areas of 100 and 10,000 m<sup>2</sup> would require temperatures of at least 1200 and 500 K, respectively, to be detected. The temperatures 1200 and 500 K represent the upper and lower thresholds for flaming and smoldering fires, respectively, in the MODIS fire algorithm (e.g., Kaufman et al. 1998b). Figure 8 also shows the predicted detection threshold for HyspIRI, and we see that the high spatial resolution of HyspIRI, relative to MODIS (60 m vs. 1 km at nadir, respectively), will improve our detection of small fires. For a fire at 500 K, the necessary area threshold drops from 10,000 m<sup>2</sup> (MODIS) to 30 m<sup>2</sup> (HyspIRI).

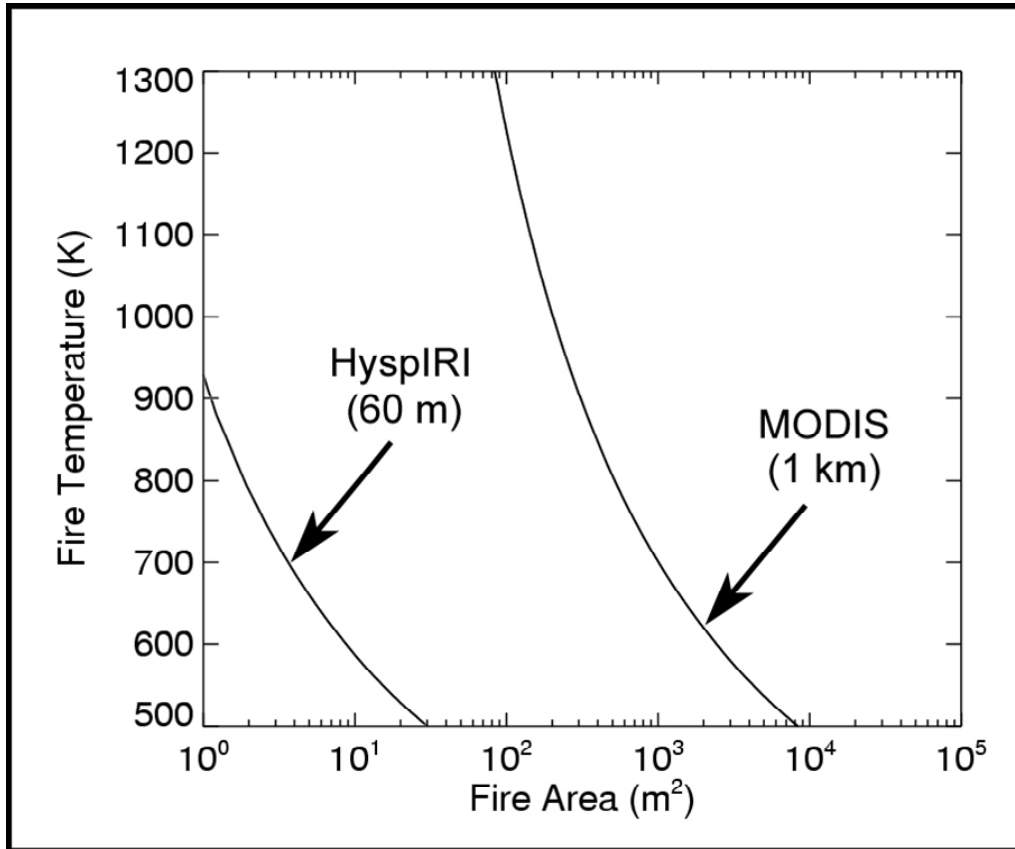


**Figure 8. Detection thresholds for the MODIS fire algorithm at the spatial resolution of MODIS and HyspIRI [data courtesy of L. Giglio].**

### 3.2 The MODVOLC Algorithm

MODVOLC is an automated hot-spot detection system developed and operated by the University of Hawaii (Wright et al. 2002, 2004). The algorithm is run on every MODIS scene, but MODVOLC is not part of the standard MODIS product generation system. Consequentially, the MODVOLC algorithm operates under strict resource restrictions. The algorithm has no context mode and is limited to eight mathematical operations on the radiance measured in five MODIS channels.

The limited computational resources available to MODVOLC preclude the conversion of radiance to brightness temperature, and the detection algorithm is based on characteristic changes in the shape of radiance spectra due to the presence of sub-pixel hot spots (Fig. 6). The increase in the radiance at 4  $\mu\text{m}$  (MODIS Ch. 21/22) relative to that at 12  $\mu\text{m}$  (Ch. 32) will decrease the difference between the radiance measured in these channels. As with the MODIS fire detection algorithm, MODVOLC makes use of Ch. 22 data preferentially, switching to Ch. 21 when Ch. 22 data are saturated.

However, the difference in radiance at 4 and 12  $\mu\text{m}$  ( $L_4 - L_{12}$ ) is also sensitive to isothermal surface temperature. As shown in Figure 9, a plot of  $L_4 - L_{12}$  vs. temperature, this relationship is not unique. For example, a radiance difference of  $-10 \text{ W m}^{-2} \text{ sr}^{-1} \mu\text{m}^{-1}$  can result from surface

temperatures of 40 or 140°C (Fig. 9). To remove this ambiguity the radiance differences are normalized by the sum of the radiances, which increases with an increase in  $L_4$ . The resulting normalized temperature index, or NTI, is weighted to surfaces with sub-pixel hot fractions.

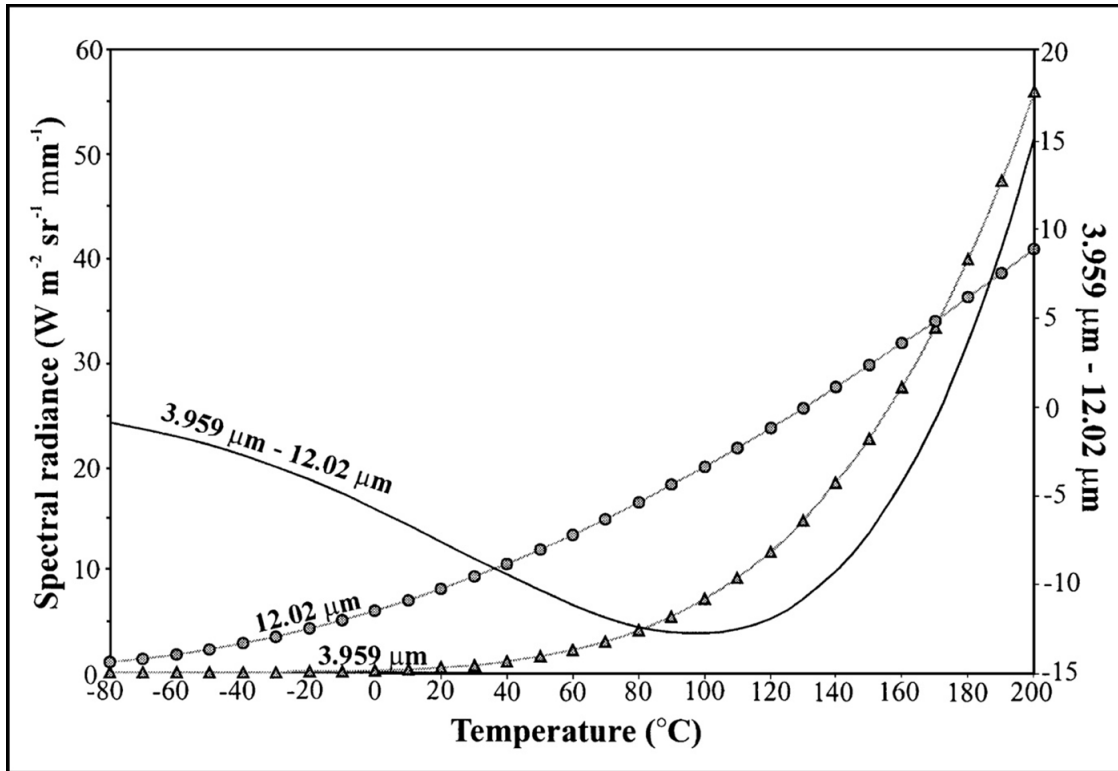


**Figure 9. Difference in radiance at 4- and 12- $\mu\text{m}$  as a function of temperature [Wright et al., 2002].**

### 3.3 Sub-Pixel Temperature Models

Dozier (1981) and Matson and Dozier (1981) pioneered the use of two-component temperature mixing models to estimate the temperature and area of the hot component. This technique was originally developed for the AVHRR instrument, utilizing the radiance measured in Channels 3 (3.55 – 3.93  $\mu\text{m}$ ) and 4 (10.5 – 11.5  $\mu\text{m}$ ). Denoting the radiance at 4  $\mu\text{m}$  (AVHRR Ch. 3) and 11  $\mu\text{m}$  (AVHRR Ch. 4) as  $L_4$  and  $L_{11}$ , respectively, the relative contributions of the high-temperature ( $T_h$ ) and background ( $T_b$ ) components to the radiance may be modeled as:

$$\begin{aligned} L_4 &= pB_4(T_h) + (1 - p)B_4(T_b) \\ L_{11} &= pB_{11}(T_h) + (1 - p)B_{11}(T_b), \end{aligned}$$

where  $p$  is the fraction of the pixel occupied by the high-temperature component and  $B_4$  and  $B_{11}$  represent the blackbody radiance at 4 and 11  $\mu\text{m}$ , respectively. In most applications, the background temperature ( $T_b$ ) is estimated from pixels surrounding the pixel of interest. Two-component temperature models have been applied to numerous studies of fires and volcanic phenomena, incorporating data from the following instruments: ASTER (Eckmann et al. 2009), AVHRR (e.g., Langaa 1993; Giglio et al. 1999; Harris et al. 1997a,b), Landsat (e.g., Wooster and Kanako 2001; Wright et al. 2001), ATSR (Wooster and Rothery 1997), and BIRD (Oertel et al. 2004; Siegert et al. 2004; Wooster et al. 2003), as well as the airborne AVIRIS (e.g., Oppenheimer et al. 1993b; Dennison et al. 2006) and Digital Airborne Imaging Spectrometer (DAIS; Lombardo et al. 2006).

However, most high-temperature events involve more than two sub-pixel temperature components, and the resulting estimates of the high-temperature component are too low. To evaluate the impact of such additional components on two-channel temperature retrievals of fire temperatures, Giglio and Kendall (2001) introduced components representing smoldering fire, at a temperature intermediate to the flaming and background temperatures, and a burned area component, at a temperature above the background temperature. Similarly, Harris et al. (1997a) introduced a third component representing hot crust, at a temperature intermediate to the melt and background temperatures, to an analysis of AVHRR data acquired during the 1991–1993 eruption of Mt. Etna. In both investigations, these additional model components provided insight into the radiative process but were not constrained by the observed data. Giglio and Kendall found that the addition of the smoldering component resulted in a systematic underestimate of the area of the flaming component. Their four-component model led to systematic underestimates of fire temperature and overestimates of fire area. The following conclusion by Giglio and Kendall is a prelude to the role of HyspIRI in studies of wildland fires:

In order to reliably determine instantaneous fire temperature and area over a wide range of active fire sizes using Dozier's two-component model, it would be necessary to observe fire activity with sensors having much higher spatial resolution (~100 m) and very high (>1000 K) middle infrared band saturation.

Various investigators have explored the use of multiple spectral channels in temperature-mixing models. Oppenheimer et al. (1993b) applied curve-fitting techniques to AVIRIS data to obtain estimates of the temperature and size of hot spots at Stromboli volcano. Harris et al. (1999) applied a three-component model to triplets of Landsat TM channels to study the temperature structure of lava lakes. Wright and Flynn (2003) and Wright et al. (2010) present a non-linear

minimization approach for estimating the temperature and fractional area of multiple sub-pixel components from Hyperion data. Dennison et al. (2006) and Eckmann et al. (2008) demonstrated that spectral mixing analysis could be used to estimate fire temperatures and area from AVIRIS and MODIS data, respectively. We employed the approaches of Wright et al. and Dennison et al. to help define the HyspIRI saturation temperature, and we discuss these approaches in greater detail in the following sections.

### 3.4 Minimized Multi-Component Modeling

The multi-component approach developed by Wright and Flynn (2003) is based on the extension of the two-component model to three or more components. To address the problem of resolving the temperature and fractional area of the additional components, the multi-component model was developed for analysis of hyperspectral V-SWIR data acquired with the Hyperion instrument. This approach allowed Wright and Flynn to treat the temperature and fractional area of each component as free parameters, in contrast to the multi-component models from Oppenheimer (1993b), Giglio and Kendall (2001), and Harris et al. (1997a,b and 1999). The strategy of the Wright and Flynn approach is to minimize the number of sub-pixel components required to fit the observed radiance spectrum.

Figure 10 illustrates the concepts behind minimized multi-component modeling. The FLIR-based temperature map represents the distribution of temperatures found within a pixel from a hypothetical satellite image data acquired over an active lava flow. The histograms to the right of the FLIR map show the temperature distribution. Superimposed on the histograms are gray bars representing the temperature components estimated by the conventional two-component, or dual-band, model and multi-component models with 2, 3, and 6 components. The height of a bar indicates the area fraction occupied a component.

For the dual-band model (Fig. 10[a]) the temperature of the hot component was fixed at 1100°C (1373 K), and the best solution to the model was a single temperature component at 500°C (773 K). The two-component solution (Fig. 10[b]) yielded components at 425 °C (700 K) and 700°C (973 K), with fractional areas ( $f_i$ ) of 0.9 and 0.1, respectively. Increasing the number of temperature components to 3 and 6 (Figs. 10[c] and 10[d], respectively) improved the fit to the observed temperature distribution. In practice, however, instrument noise limits the maximum number of free components to 3.

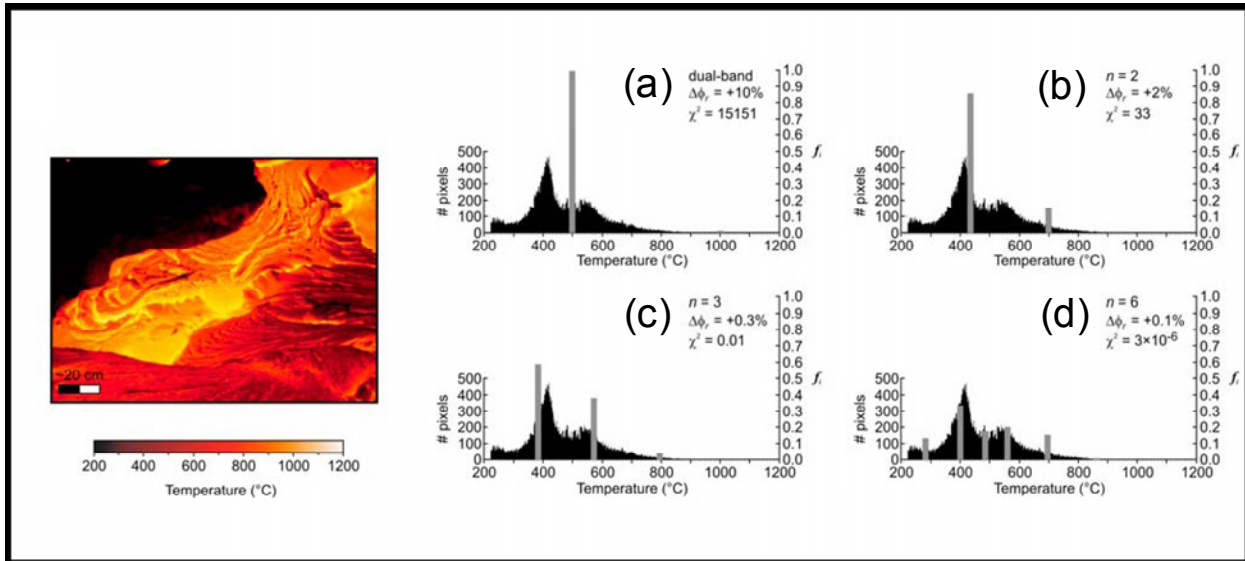


**Figure 10. Illustration of the Minimized Multi-Component Modeling technique. The FLIR image (at left) represents the distribution of temperatures within a Hyperion pixel. The histograms (at right) show the temperature distribution, together with fits of the dual-band and multi-component model results to the observed temperature distribution. The six-component model ( $n = 6$ ) yields the best fit, in the Chi-Squared ( $\chi^2$ ) sense, to the observations [Wright et al., 2010].**

### 3.5 Spectral Endmember Mapping

Multiple endmember spectral mixture analysis (MESMA), as described by Roberts et al. (1998), fits observed spectra with linear combinations, or mixtures, of endmember spectra selected from spectral libraries. The endmember spectra, and relative contribution of the spectra to the spectral mixture, are treated as free parameters and may vary from pixel to pixel. Dennison et al. (2006) demonstrated that the MEMSA concept could be extended to map fire temperatures and fractional areas. The investigators introduced a new spectral library of emitted radiance, containing synthetic spectra generated for representative ground cover types and temperatures between 500 and 1500 K. The observed radiance was modeled as a combination of solar reflected radiance, emitted radiance, and shade (or zero radiance). The solar-reflected radiance endmembers were selected from the image data under consideration.

Figure 11 contains the fire temperature and fractional area estimates derived from AVIRIS data acquired over the 2003 Simi Fire, which burned ~44,000 ha (440 km<sup>2</sup>) in the Santa Susana Mountains of Ventura County, California. Figure 11(a), a false-color composite of AVIRIS data collected at 1.682, 1.107, and 0.655  $\mu\text{m}$ , displayed in red, green, and blue, respectively, shows the locations of the active fire fronts. Figure 11(b), the map of fire temperature, indicates that temperatures along the active fronts were as high as 1100 K. Figure 11(c), the map of fire fractional areas, indicates that the highest temperatures shown in Figure 11(b) corresponded with fractional areas as high as 95%.

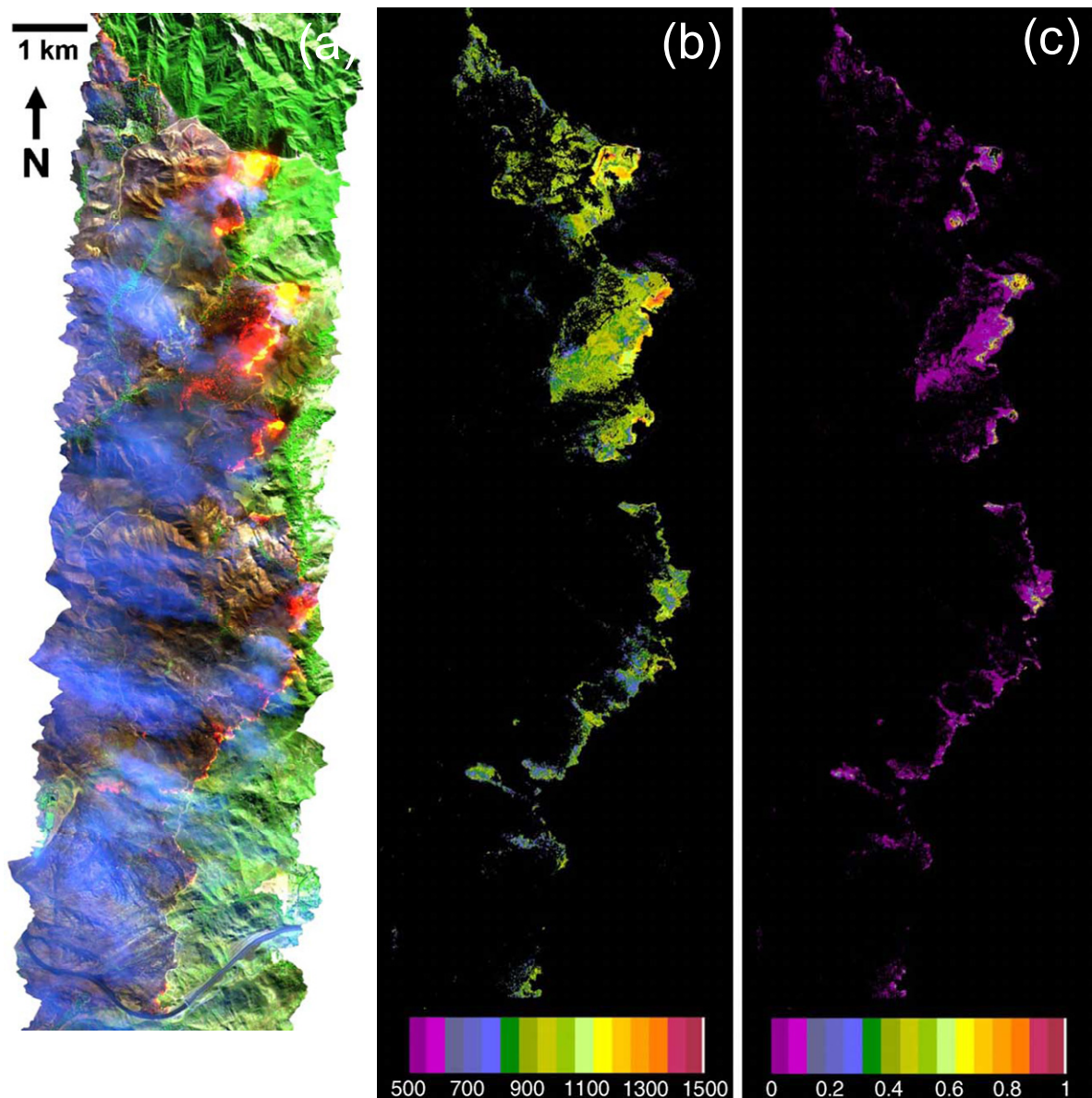


**Figure 11. Results of the application of Multiple Endmember Spectral Mixture Analysis (MEMSA) to AVIRIS data from the 2003 Simi Fire. (a) Color-composite of data from the 1.682, 1.107, and 0.655  $\mu\text{m}$  channels of AVIRIS; (b) map of fire temperatures; and (c) map of fractional areas corresponding to the fire temperatures [Dennison et al., 2006].**

### 3.6 Fire Radiant Power

While the sizes and temperatures of hot spots are important information for studies of wildfires, these parameters tell us little about the amount of fuel (biomass) consumed, or mass of carbon volatized, by a fire. The fire radiant power (FRP) is an instantaneous measure of the radiant energy released by combustion, per unit area, that can be derived via remote sensing. The integral of FRP over the life of a fire gives us the fire radiant energy (FRE), which is proportional to the total amount of biomass consumed by the fire (Kaufman et al. 1998a,b,c; Wooster et al. 2003 and 2005; Roberts et al. 2005).

The theoretical form of FRP is based on the Stefan-Boltzmann Law, which is the integration of the Planck Law over wavelength and solid angles. The Stefan-Boltzmann Law describes the radiant flux per unit area ( $\text{W m}^{-2}$ ) corresponding to a temperature  $T$ :

$$M = \sigma T^4,$$

where  $\sigma$  is the Stefan-Boltzmann constant ( $5.67 \times 10^{-18} \text{ J s}^{-1} \text{ m}^{-2} \text{ K}^{-4}$ ). For a fire with multiple temperature components, the FRP may be expressed as:

$$FRP = \varepsilon \sigma \sum_{i=1}^n A_i T_i^4,$$

where  $n$  is the total number of temperature components,  $A_i$  and  $T_i$  are the fractional area and temperature, respectively, of the  $i^{\text{th}}$  component, and  $\varepsilon$  is the (broadband) emissivity of the fire. If there are only two temperature components, fire plus background, then the standard two-component temperature retrieval techniques can be used to estimate  $A_i$  and  $T_i$ . In practice, however, the FRP is derived via empirical functions of the 4- $\mu\text{m}$  temperature ( $T_4$ ), such as the approximation developed by the MODIS Fire Team (e.g., Kaufman et al. 1998a and 1998b):

$$FRP \approx 4.34 \times 10^{-19} (T_{4,f}^8 - T_{4,b}^8),$$

where  $T_{4,f}$  and  $T_{4,b}$  indicate the 4- $\mu\text{m}$  temperatures of the fire and background, respectively. The difference between the fire and background temperatures provides an approximation of the “excess radiance” generated by the fire.

The chief advantage of the MODIS FRP estimation technique is its simplicity—the estimation is based on radiance measured in one spectral channel. To extend this advantage to data acquired with other instruments, Wooster et al. (2003 and 2005) have developed a more generalized estimation procedure. The first step in the development of this technique was to approximate the 4- $\mu\text{m}$  radiance ( $L_4$ ) with a simple power law:

$$L_4 \approx aT^4$$

that holds for temperatures in the range between 650 and 1300 K. The coefficient  $a$  is a function of the band-pass of the 4- $\mu\text{m}$  channel and, with the notable exception of the BIRD HSRS ( $a = 3.33$ ), this coefficient may be approximated as  $3 \times 10^{-9}$  (Wooster et al. 2005). The use of the

power law approximation for radiance results in a simplified model that does not require knowledge of the fire or background temperatures:

$$FRP \approx \frac{A\sigma}{(3 \times 10^{-9})} (L_{4,f} - L_{4,b}),$$

where  $A$  is the projection of the instrument IFOV onto the surface,  $\sigma$  is the Stefan-Boltzman constant, and  $L_{4,f}$  and  $L_{4,b}$  are the radiance of the fire and background, respectively, at 4  $\mu\text{m}$ . Applications of the simplified FRP model to BIRD, SEVIRI, and GOES data are found in Wooster et al. (2003), Roberts et al. (2005), and Pereira et al. (2009), respectively. We use the FRP approach to help define the HyspIRI saturation temperature, and we will return to our discussion of this approach in a later section.

## 4 Case Studies

---

Our specification of saturation temperature is based on a review of the literature and analyses of airborne and satellite data from five case studies. As discussed in the previous sections, the presence of multiple temperature components within a pixel results in temperature estimates that depend strongly on the spatial and spectral resolution of the radiance measurements. Our case studies are based on radiance measurements at spatial resolutions  $< 60$  m aggregated to 60-m, or HyspIRI, resolution prior to the estimation of temperature. This strategy gave us explicit knowledge of the extent of sub-pixel mixing. For the published temperature estimates, we gave preference to estimates derived from radiance measurements at spatial resolutions  $> 60$  m that included estimates of the area of the hot component. This strategy allowed us to determine if the hot component would fill a HyspIRI pixel.

### 4.1 Published Studies

Without access to the original radiance data, we cannot aggregate the published temperature estimates derived from radiance measurements at high spatial resolution ( $< 60$  m) to HyspIRI resolution. However, such estimates provide a useful perspective on the variability of high-temperature phenomena. For example, Wooster et al. (2005) reported temperature estimates up to 1650 K for an experimental fire beneath an 11.5-m observation tower. These temperature estimates were derived from data acquired with a non-imaging spectro-radiometer. Riggan et al. (1993 and 2004) described the use of an airborne IR scanner to measure temperatures in the range 1400–1600 K for leading edges of controlled burns in the Brazilian savanna. Temperatures within the fires were in the range 900–1200 K, and the trailing edges were  $< 900$  K. Dennison et al. (2006) applied spectral endmember mapping to AVIRIS data acquired over a wildland fire in Southern California and estimated fire temperatures as high as 1500 K, with the majority of temperatures in the range 750–950 K. Eckmann et al. (2009) estimated fire temperatures up to 1500 K through an application of spectral endmember mapping to ASTER data.

Examples of temperature estimates for volcanic phenomena include Rose and Ramsey (2009), who derived temperature estimates of  $\sim 1080$  K from ASTER VNIR data acquired over open-channel lava flows from Klyuchevskoy Volcano. Wooster et al. (2000) reported temperatures up to  $\sim 1100$  K for the active lava dome at Unzen lava dome, derived from Landsat TM data acquired in 1991 and 1992. Vaughan et al. (2008) estimated temperatures up to  $\sim 825$  K for carbonate-rich lava flows at Oldoinyo Lengai Volcano based on analysis of ASTER data.

Turning to surveys conducted at low spatial resolution, Harris et al. (1995a) found that  $240,000$  m $^2$  of a lava flow emplaced during the 1984 eruption of Krafla Volcano was at a temperature of  $\sim 1325$  K. This expansive hot spot, mapped with AVHRR data, would contain over 65 HyspIRI pixels. The two-component temperature modeling performed by Harris et al. is similar to the dual-band approach discussed by Wright and Flynn (2003) and Wright et al. (2010); the temperature of the hot component was fixed at 1325 K, and the area of this component and the background temperature were estimated from the observed radiance. Eckmann et al. (2008) applied spectral endmember mapping to MODIS data acquired over wildland fires in the Ukraine and found several pixels containing components at 500 K that were large enough to fill a HyspIRI pixel. The investigators validated the size of the hot components through comparison with coincident ASTER SWIR data.

As shown in Table 1 and Figure 2, the BIRD HSRS provided 4- $\mu\text{m}$  radiance measurements with the highest spatial resolution (370 m) and saturation temperature (600 K) of the heritage instruments. Based on these attributes, the published results from HSRS are strong predictors of the potential results from HyspIRI. The lifespan of the BIRD mission was brief—BIRD was launched on October 22, 2001, and operations ceased on December 31, 2005.

Table 2 is a summary of HSRS results drawn from Briess et al. (2003), Oertel et al. (2004), Siegert et al. (2004), and Zhukov et al. (2006). The areas corresponding to the high-temperature features are given in hectares; for the purpose of comparison with HyspIRI, we note that a 60-m HyspIRI pixel ( $3600 \text{ m}^2$ ) is equal to 0.36 hectares. All of the features listed in Table 3 were large enough to fill at least one HyspIRI pixel. The largest feature in this table, a lava flow of Mt. Etna, would fill 69 HyspIRI pixels. The HSRS results suggest that the HyspIRI saturation temperature should be no lower than 1000 K.

**Table 2. Temperature Estimates Derived from BIRD HSRS Data**

Australia Fire 2002-01-05		Kalimantan Fire 2002-08-24/25		Lake Baikal Fire 2003-06-16		Etna Lava Flow 2002-11-02	
T <sub>f</sub> (K)	A <sub>f</sub> (Ha)	T <sub>f</sub> (K)	A <sub>f</sub> (Ha)	T <sub>f</sub> (K)	A <sub>f</sub> (Ha)	T <sub>f</sub> (K)	A <sub>f</sub> (Ha)
815	0.48	860	2.5	800 - 920	4.4 - 8.4	540	25
715	2.3	740	1.9	668 - 771	0.7 - 1.5	-	-
893	0.59	650	4.6	716 - 868	1.2 - 3.1	-	-
852	0.92	520	2.1	740 - 839	0.38 - 0.71	-	-
957	1.0	720	1.1	771 - 988	0.23 - 0.70	-	-
796	0.39	690	3.0	819 - 913	1.4 - 2.3	-	-
-	-	590	3.3	694 - 882	0.36 - 1.21	-	-
-	-	560	0.7	-	-	-	-

## 4.2 Team Studies

### 4.2.1 AMS Survey of Southern California Wildfires

In this section, we present an analysis of data acquired with the Autonomous Modular Sensor (AMS) during the Southern California Firestorm of October 2007. The AMS, which is operated by the NASA/Ames Research Center (ARC), was deployed on the Ikhana UAV platform. Figure 12 lists the specifications for the AMS, which was configured in high-temperature mode for the Southern California missions. This configuration included spectral channels between 3.60 and 3.79 (Channel 11) and 10.26 and 11.26  $\mu\text{m}$  (Channel 12). The AMS data were acquired between October 24 and 28; there were no flights on October 27 due to cloudy weather conditions.

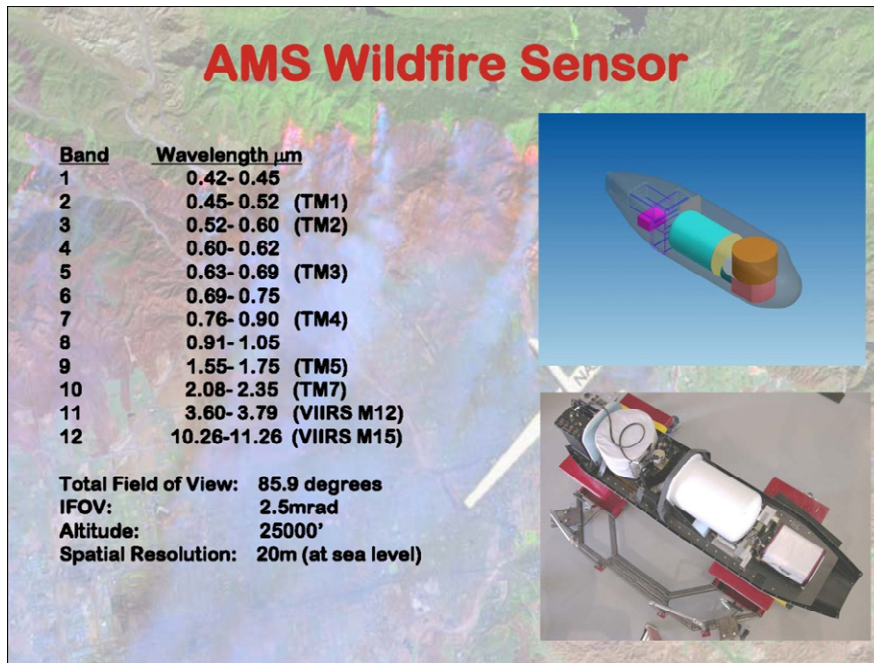


**Figure 12. Characteristics of the Autonomous Modular Sensor (AMS), together with photograph showing instrument as mounted in a wing pod [courtesy NASA ARC/ASF].**

Figure 13 is a map showing the locations of Southern California fires as of November 9, 2007, following the final containment of the fires. The text boxes outlined in red describe the five fires studied in this report. Table 3 summarizes this information, together with the number of AMS flights over the study areas. Listed from north to south, our study included the Grass Valley, Santiago, Poomacha, Witch, and Harris Fires (Fig. 13). The Witch Fire was the largest and most destructive fire; the Grass Valley Fire was the smallest, in terms of burn area, but the damage to structures was large in proportion to the small size of this fire.

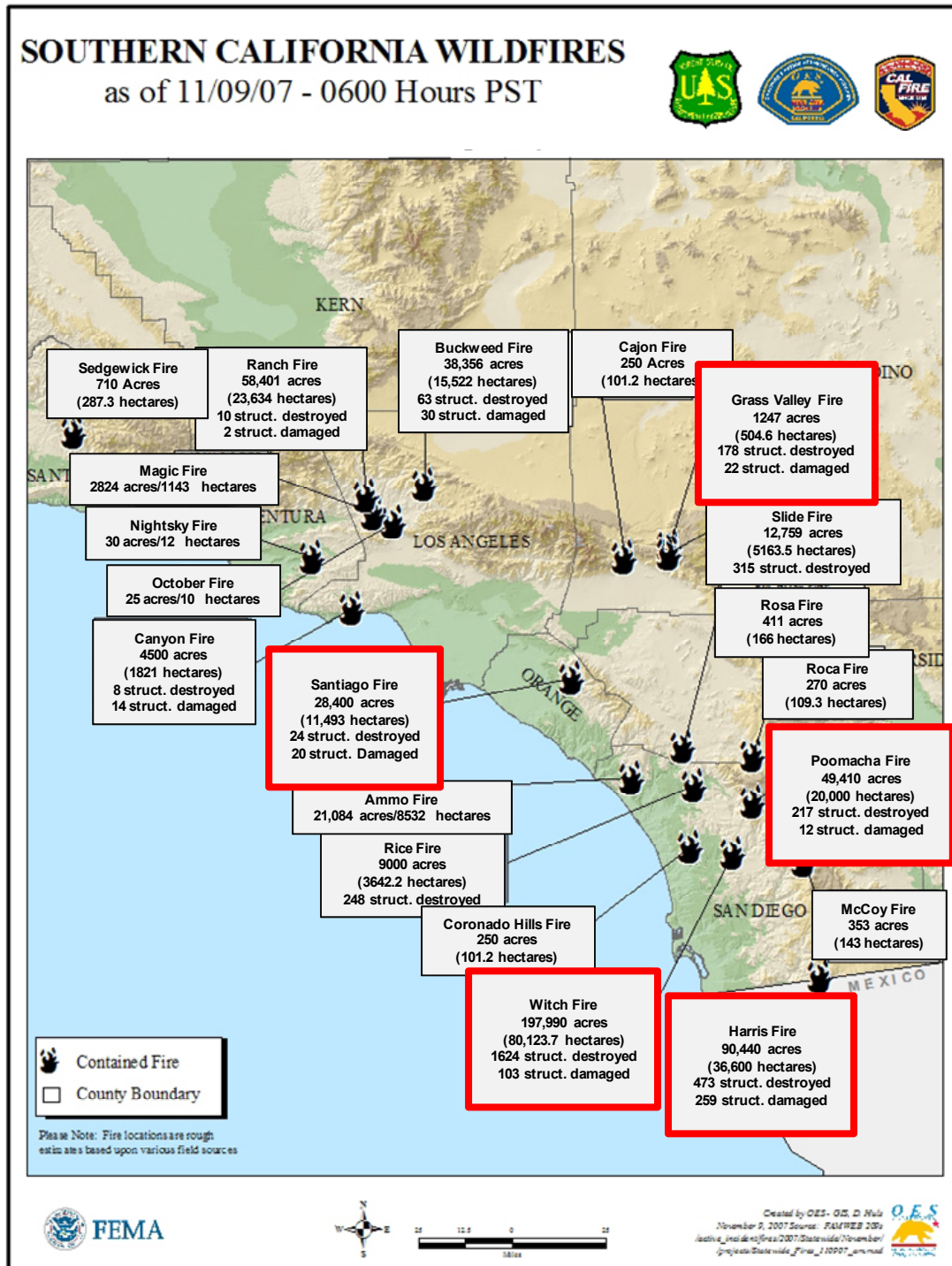


**Figure 13. Locations of Southern California Wildfires as of 9 November 2007, following the final containment of these fires. The text boxes outlined in red describe the fires studies in this report.**

**Table 3. Statistics for the Wildfires Described in Case Study**

Name	Burn Area		Structures Damaged or Destroyed	AMS Flight Line Count
	Acres	Hectares		
Grass Valley	1247	505	200	25
Santiago	28,000	11,500	44	9
Poomacha	49,000	20,000	229	19
Witch	198,000	80,000	1727	26
Harris	90,000	37,000	732	15

### Analysis Procedure

We obtained the AMS data from the Airborne Sensor Facility (ASF) at ARC. These data are available as HDF files, containing several data fields in addition to the radiance data. For this study we extracted the longitude, latitude, surface elevation (DEM) and sensor zenith angles for each image pixel from the ancillary data fields.

The first step in our analysis was a visual inspection of the radiance data to identify the flight lines that covered active fire fronts, with an emphasis on flight lines that were centered on fire fronts. This emphasis was necessitated by the difference between the total Field of View (FOV) of AMS ( $85^\circ$ ) and HyspIRI ( $51^\circ$ ). To approximate the effects of atmospheric absorption and emission on HyspIRI measurements, we restricted our analysis to AMS pixels within  $\pm 26^\circ$  of nadir.

We used the pixel latitude and longitude data to project the AMS data into UTM coordinates and then aggregated the radiance data to the 60-m spatial resolution of HyspIRI. The map projection and aggregation operations were applied to floating point values to minimize the effects of resampling and interpolation on the simulated radiance. Finally, we converted the simulated HyspIRI radiance to brightness temperature.

Figure 14 demonstrates of the impact of spatial resolution on our temperature estimates. At high spatial resolution, the probability that the surface, or target, within a pixel is isothermal is also high. With decreasing spatial resolution, there is an increase in the probability of sub-pixel temperature mixing and a decrease in the fractions of a pixel occupied by hot components. If sub-pixel hot spots are present, the general effect of decreasing spatial resolution is a decrease in the pixel-integrated temperature.

The data depicted in Figure 14 were acquired over the Santiago Fire on October 26, 2007. Figure 14(b) is a map of 3.7- $\mu$ m (Channel 11) brightness temperatures at a spatial resolution of 8.3 m (following the re-projection to UTM coordinates). Figures 14(c) and (d) show the results of re-sampling the AMS data to the 60-m spatial resolution of HyspIRI and 1-km resolution of MODIS, respectively. We note that the high-temperature estimates at HyspIRI resolution (Fig. 14[c]) are approximately 25 K lower than the original estimates (Fig. 14[b]), but the relative distribution of temperature within the active fire fronts are preserved in the simulated HyspIRI scene. At the 1-km spatial resolution of MODIS (Fig. 14[d]), the high-temperate estimates are 100 K lower than the original estimates (Fig. 14[b]), and we have lost any information regarding the spatial distribution of temperature with the fire fronts.

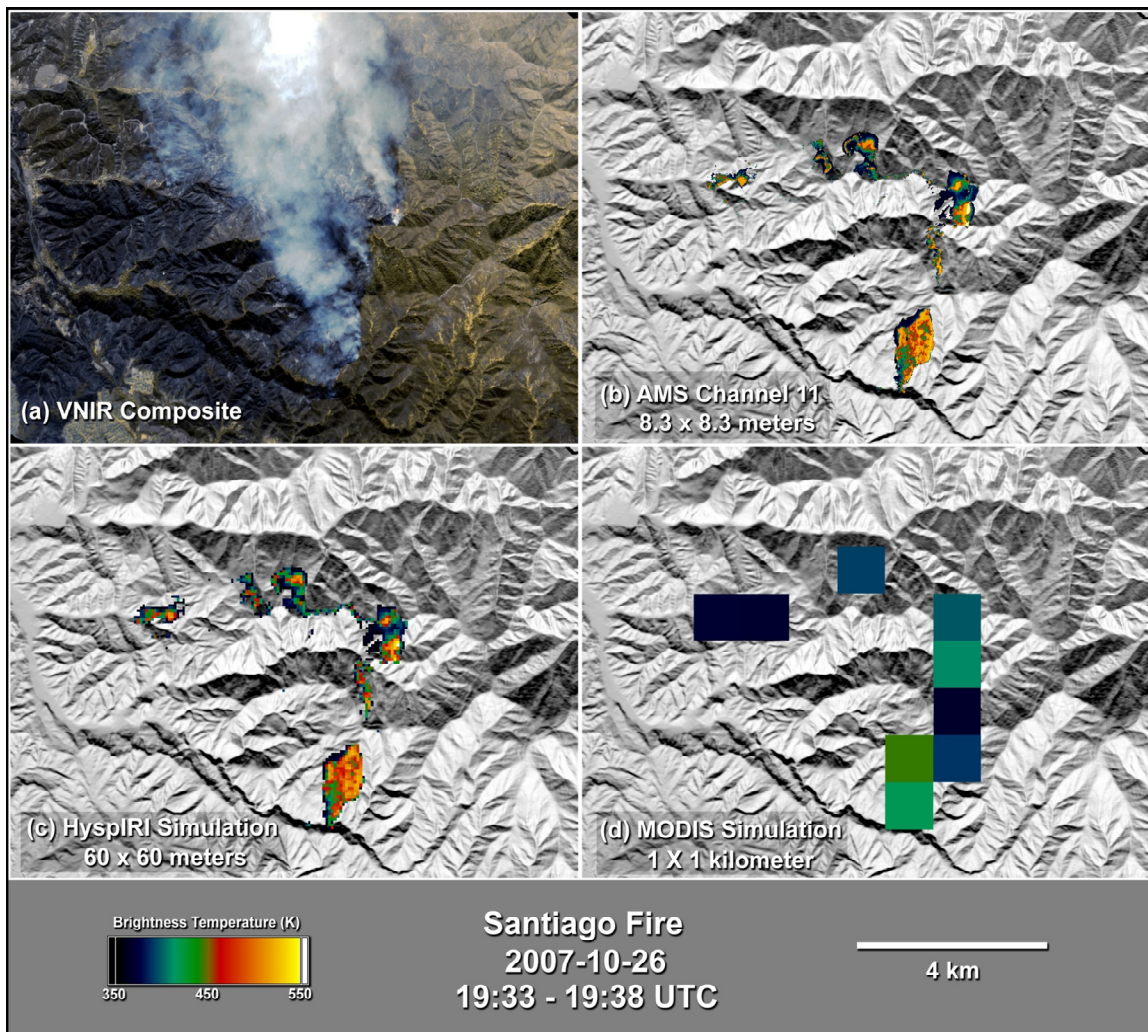


**Figure 14. Impact of spatial resolution on the perceived temperature of a pixel.** (a) Color-composite of AMS VNIR data; (b) 4- $\mu$ m temperature at native AMS resolution (8.3 meters); (c) temperature at HyspIRI resolution (60 meters); and (d) temperature at MODIS resolution (1 km).

Our original intent for this case study was to use the aggregated AMS 3.7- $\mu\text{m}$  radiance data to predict the maximum 4- $\mu\text{m}$  radiance that HyspIRI might encounter over a wildland fire. However, we could not follow this approach due to saturation of the 3.7- $\mu\text{m}$  (Channel 11) radiance data. As shown in Figure 15, a scatterplot of brightness temperatures for the 3.7- and 10.5- $\mu\text{m}$  channels (Channels 11 and 12, respectively), the 3.7- $\mu\text{m}$  temperatures did not exceed 530 K. However, the scatterplot results suggested that we could use the 10.5- $\mu\text{m}$  (Channel 12) data to measure temperatures up to 800 K. Laboratory calibration of AMS, performed in 2008 (Fig. 16), confirmed the saturation of the 3.7- $\mu\text{m}$  channel and the lack of saturation in the 10.5- $\mu\text{m}$  channel. The calibration of the 10.5- $\mu\text{m}$  channel revealed a temperature-dependent bias that we accommodated with the following linear correction:  $T_{\text{true}} = (T_{\text{est}} - 71\text{K})/0.8175$ .

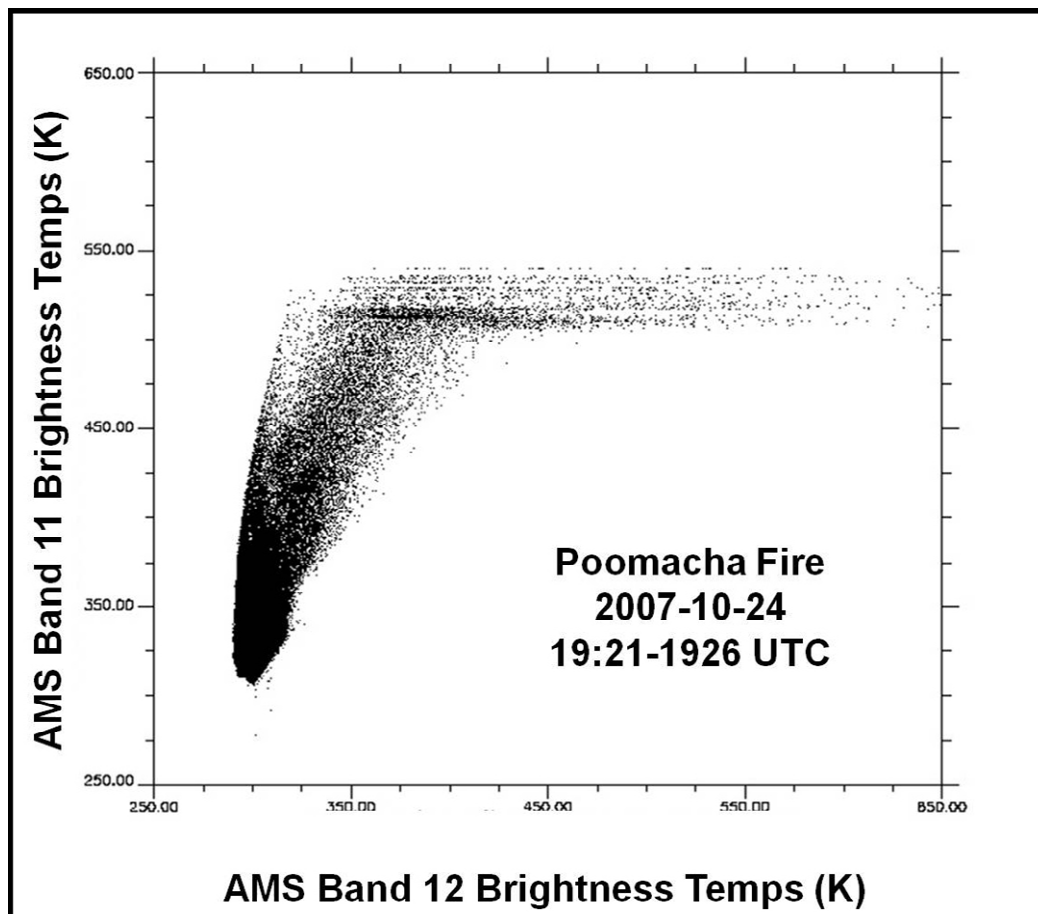


**Figure 15. Scatterplot of brightness temperatures in AMS Channel 11 (3.7  $\mu\text{m}$ ) vs. Channel 12 (10.5  $\mu\text{m}$ )**

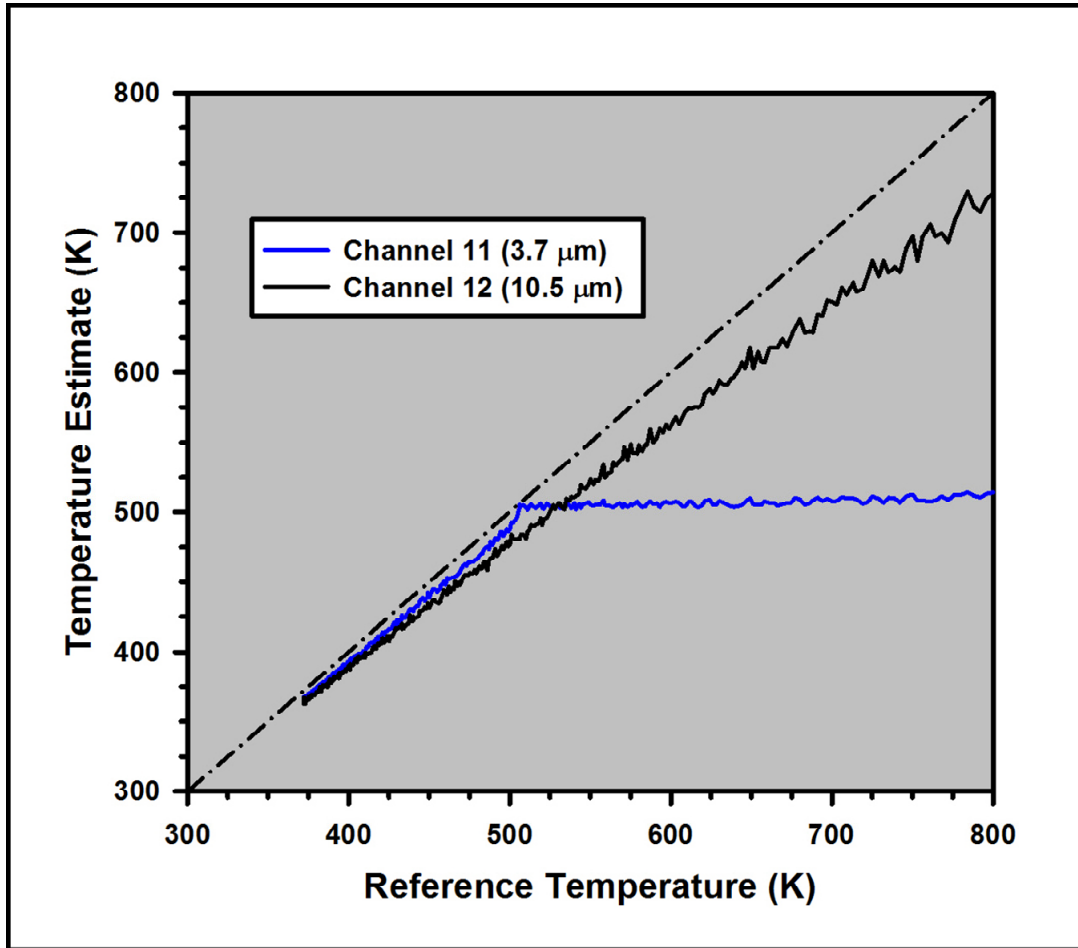


**Figure 16. Laboratory calibration of AMS Channels 11 and 12. Dashed line indicates perfect agreement between reference and estimated temperatures. Temperature-dependent bias in the Channel 12 response modeled as  $T_{ref} = (T_{est} - 71K)/0.8175$  [courtesy NASA/ARC ASF].**

Figure 17 is a collection of histograms showing the probability distribution of the hot temperatures ( $330 \leq T \leq 730$  K) for each study area, following aggregation of the 10.5- $\mu\text{m}$  radiance data from native resolution to 60-m HyspIRI-scale pixels. We see that the probability distribution for all fires (Fig. 17[a]), is dominated by the Poomacha Fire (Fig. 17[b]), which contributed approximately 60% of the pixels to the total. We note that the Witch Fire (Fig. 17[e]) contributed only 7.4% of the pixels to the total. The sizes of these contributions appear to be counterintuitive, as the area burned by the Witch Fire was more than four times larger than the area burned by the Poomacha Fire. Fire science is beyond the scope of this report, and additional research will be required to determine if this negative correlation between total burn area and fire temperature was the result of environmental factors, such as available fuel loads or local topography, or a bias imposed by the logistics of deploying the Ikhana UAV platform. For example, the Ikhana may not have surveyed the hottest portions of the Witch Fire due to scheduling or airspace restrictions.

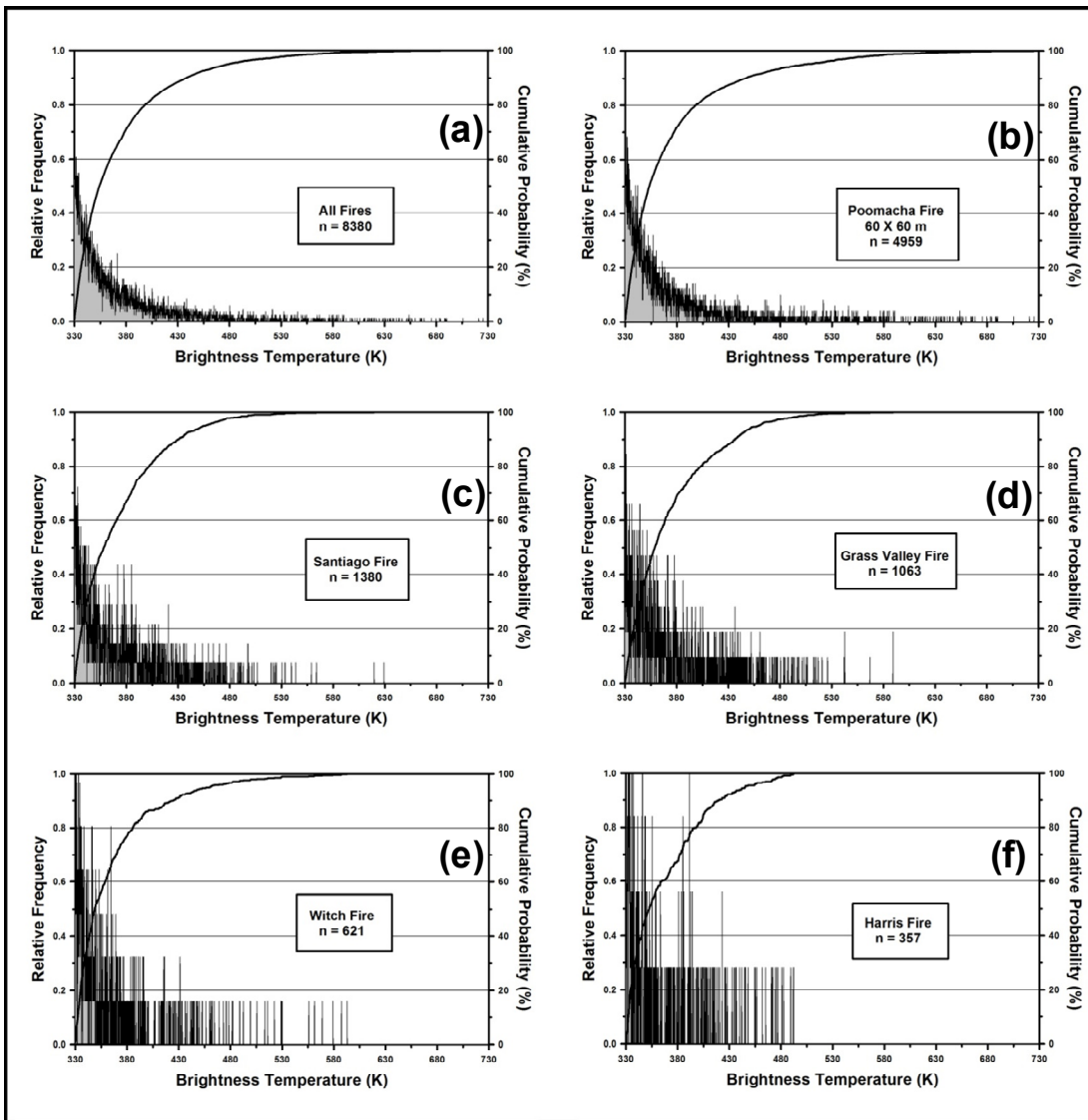


**Figure 17. Relative frequency and cumulative histograms of high temperatures estimates (330 – 730 K), following aggregation of the Channel 12 (10.5  $\mu$ m) radiance from native resolution into 60-m HyspIRI pixels. (a) Histogram for all fires; (b) Poomacha Fire histogram, (c) Santiago Fire histogram; (d) Grass Valley Fire histogram; (e) Witch Fire histogram; and (f) Harris Fire histogram.**

We will focus our attention on the Poomacha data since the data depicted in Figure 17 suggest that the Poomacha histogram could be used as a proxy for the all-fire histogram. The maximum temperature at 60-m resolution was 795 K, following the application of our linear correction. As we saw in Figure 14, the high spatial resolution of HyspIRI will minimize the effects of sub-pixel temperature mixing.

To evaluate the impact of sub-pixel mixing on the maximum temperature estimate, we compared the cumulative histograms of the temperatures at native and aggregated (60-m) resolution. This comparison is found in Figure 18, where Figs. 18(a) and 18(b) are the histograms for the native and aggregated 60-m resolution, respectively, and Fig. 18(c) is the comparison of cumulative histograms. We see that the cumulative histograms diverge for temperatures higher than 380 K, corresponding to a cumulative probability of 60%. For temperatures higher than 380 K, the native-resolution temperatures are higher than the corresponding 60-m temperatures at probabilities greater than 60%, although the separation between the cumulative histograms is less than 5%.

The agreement between the cumulative histograms (Fig. 18[c]) indicates that the 60-m temperature distribution maintained much of the structure of the native distribution, but sub-pixel temperature mixing was a factor for pixel-integrated temperatures greater than 380 K. Therefore, the maximum aggregated temperature of 795 K must be a lower bound on the HyspIRI saturation temperature.

#### **4.2.2 AGEMA Camera Data for Sharpsand Creek Fire**

The Sharpsand Creek fire was a prescribed burn conducted via collaboration between the Canadian Forest Service and the Ministry of Natural Resources, with scientists from King's College London, University of Edinburgh, and University of Leicester attending from the UK. The burn site was 1 hectare (approximately 100 m x 100 m square) of Jack Pine forest located approximately 60 km north of Thessalon, Ontario, Canada (latitude 46° 47' N, longitude 83° 20' W). Smith et al. (2009) describe the Sharpsand Creek site and the prescribed burn, which occurred on May 13, 2007.

The plot was lit with a perimeter ignition pattern, which resulted in some extreme fire behavior, including flames estimated to be > 100-m high at the maximum. During the fire, a helicopter hovered above and slightly to the side of the plot, and IR imagery of the fire was collected using an AGEMA-550 thermal imaging camera equipped with a 3.9- $\mu$ m narrowband filter. The pixel brightness temperature measurements were used to calculate FRP per pixel, using the MIR approximations discussed previously (Wooster et al. 2003 and 2005). Detailed discussions of the use of AGEMA-550 data in FRP calculations are provided by Wooster et al. (2005) and Freeborn et al. (2008).

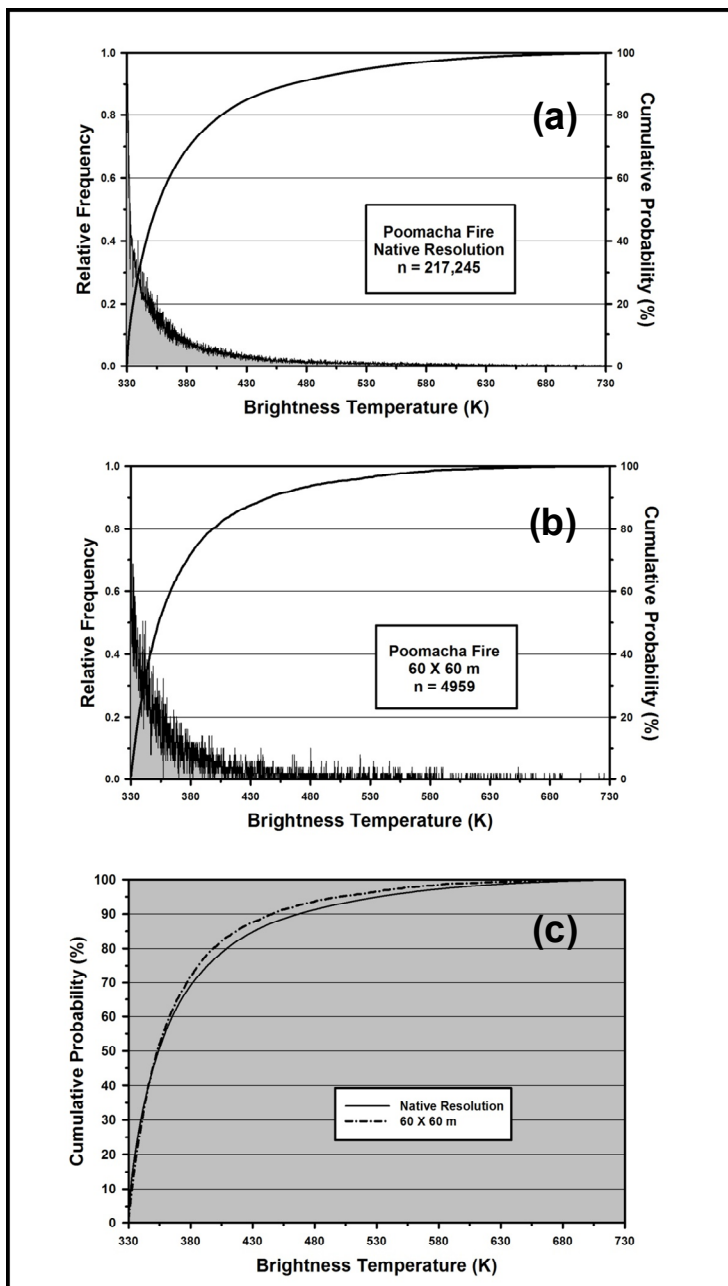


**Figure 18. Comparison of Poomacha Fire temperatures at the spatial resolutions of AMS and HyspIRI. (a) histograms for temperatures at native (AMS) resolution; (b) histograms for temperatures at aggregated 60-m (HyspIRI) resolution; and (c) comparison of the cumulative histograms for native-resolution (solid line) and aggregated (dashed line) temperatures.**

Figure 19 shows the spatial distribution of FRP generated from the AGEMA-550 data. We evaluated the potential HyspIRI response to this fire with two approaches. In the first approach, we aggregated the FRP over a 60 x 60-m ( $3600\text{ m}^2$ ) region of interest centered over the hottest portion of the fire. Recalling the similarity between FRP and the Stefan-Boltzmann Law, we can convert the aggregated FRP,  $\sim 430$  MW, into an apparent temperature of  $\sim 1205$  K. Our second approach was to aggregate the radiance measurements over the same region of interest and convert this aggregated radiance to an apparent temperature. The aggregated radiance,  $\sim 7454\text{ W m}^{-2}\text{ sr}^{-1}\text{ }\mu\text{m}^{-1}$ , corresponds to an apparent temperature of  $\sim 1260$  K. The two temperature estimates are within 5% of each other, and this close agreement is a validation of the approximations entailed in the FRP approach.

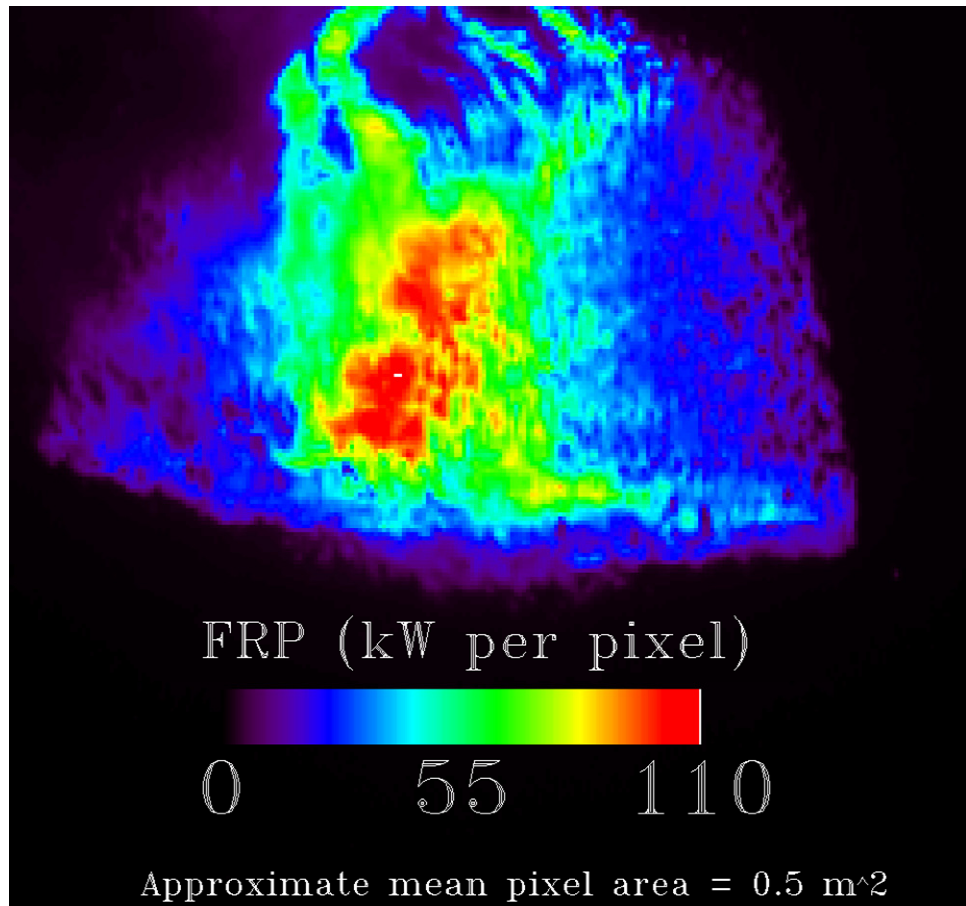


**Figure 19. Map of Fire Radiant Power (FRP) estimated for the Sharpsand Creek (Ontario, Canada) prescribed burn. Temperature estimates of 1205 and 1260 K obtained by aggregating the FRP and radiance, respectively, over a 60X60 m region of interest centered on the hottest portion of the fire [data courtesy of M. Wooster].**

#### 4.2.3 AVIRIS Survey of the Indians Fire

The Indians Fire burned a 300-km<sup>2</sup> area of Santa Lucia Mountains, Los Padres National Forest (Monterey County, California). The fire began on June 8, 2008, with final containment on July 10, 2008, and was imaged by AVIRIS and the MODIS/ASTER (MASTER) airborne simulator on June 11. Dennison and Matheson (2011) present a detailed analysis of these AVIRIS and MASTER data.

Figure 20 depicts fire temperatures and corresponding fractional areas derived through the application of the MESMA procedure to the AVIRIS data. The AVIRIS radiance data were aggregated to a spatial resolution of 64 m from the native spatial resolution of 16 m. Following the procedure established by Dennison et al. (2006), the aggregated radiance was modeled as a combination of solar-reflected radiance, emitted radiance, and shade (or zero radiance). The emitted radiance library represented temperatures between 500 and 1500 K, with each spectrum corresponding to a single temperature.

Figure 20(a) is a color-composite of the AVIRIS data acquired at 1.672, 0.957, and 0.655  $\mu\text{m}$ , displayed in red, green, and blue, respectively. The color-composite scene shows the AVIRIS data at native (16-m) resolution. Figures 20(b) and 20(c) are the maps of fire temperature and corresponding area fraction, respectively. Using the area fraction map as a guide, we identified the pixels with an area fraction of 1.0 as well as the temperatures corresponding to these isothermal pixels. Figure 20(d) plots the temperatures of the 14 isothermal pixels found in our analysis. There were six pixels with temperatures greater than 760 K, including a single pixel at 860 K. A visual inspection of Figures 20(b) and 20(c) suggests that there were a large number of pixels with area fractions only slightly less than 1.0, and many of these pixels were at temperatures between 750 and 1000 K.

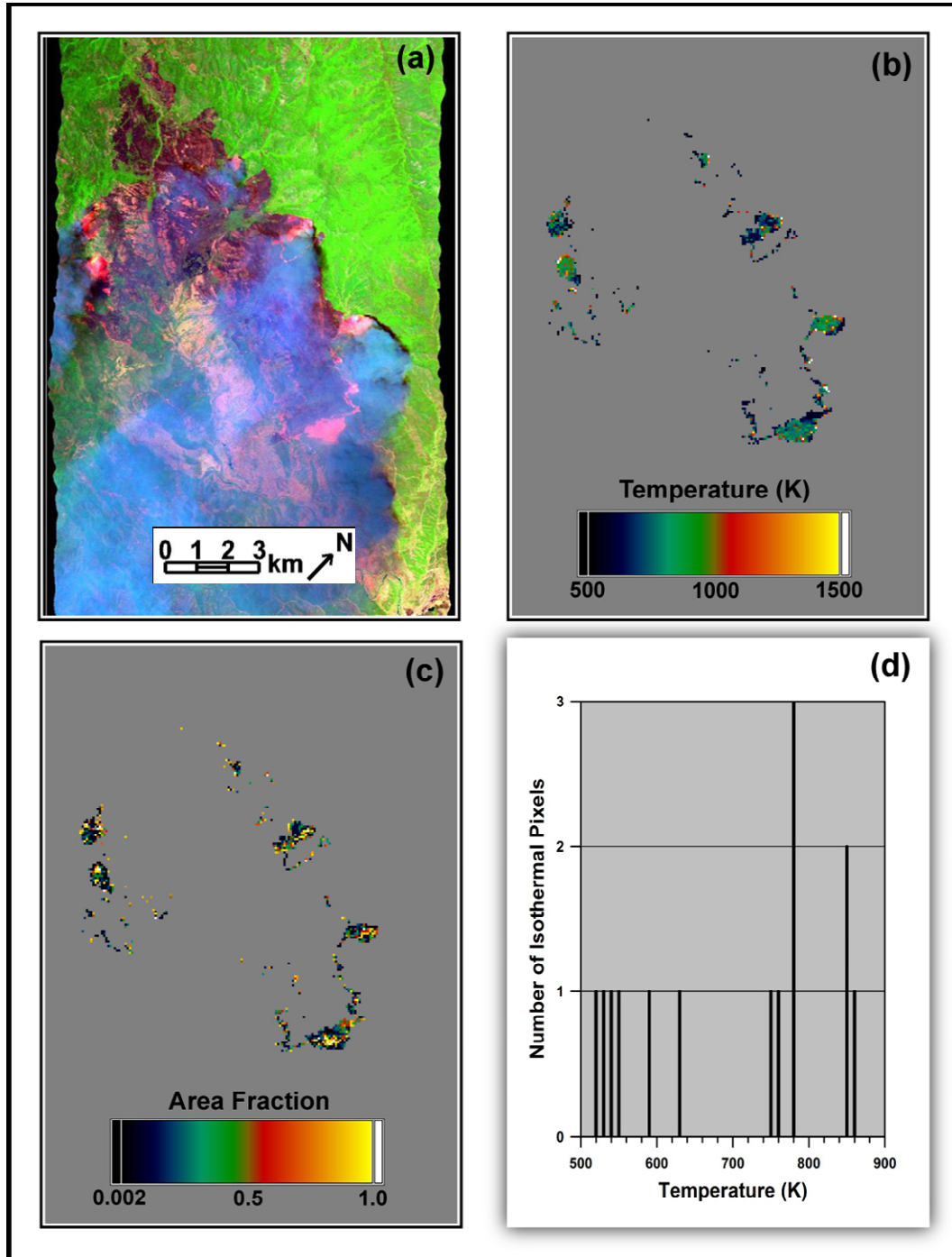


**Figure 20.** Analysis of AVIRIS data acquired over the 2008 Indians Fire, Monterey County, California. (a) Color-composite of AVIRIS data from the 1.672, 0.957, and 0.655  $\mu\text{m}$  channels; (b) fire temperature derived from application of the MESMA procedure to aggregated AVIRIS pixels; (c) area fractions corresponding to the fire temperatures; and (d) plot of the temperatures of isothermal pixels (area fraction = 1) [data courtesy of P. Dennison].

#### 4.2.4 ASTER Surveys of Klyuchevskoy and Kilauea Volcanoes

ASTER data acquired by the VNIR and SWIR subsystems feature spatial resolutions of 15 and 30 m, respectively, and radiance measurements in the VNIR and SWIR may be aggregated into HyspIRI-scale pixels. Figure 21 contains ASTER data acquired over Klyuchevskoy Volcano (Kamchatka Peninsula, Russia) on May 28, 2007, during an eruption episode that began on February 15, 2007, and ended on July 15, 2007. The color-composite of VNIR data (Fig. 21[a]) reveals an incandescent lava flow within the shadow cast by an eruption plume. This lava flow was hot enough to saturate the SWIR measurements. Fortunately, the aforementioned shadow minimized the reflection of incident solar irradiance and thus facilitated the estimation of lava flow temperatures from the VNIR data. We applied an additional correction for reflected solar irradiance, following the procedure of Wooster and Kaneko (2001).

The twin panels below the VNIR color-composite are maps of lava flow temperatures derived from radiance measured in ASTER Channel 3 (centered at  $0.807\text{ }\mu\text{m}$ ). Figure 21(b) shows the temperatures derived from the radiance at the native spatial resolution (15 m), and Figure 21(c) shows the temperatures derived from radiance aggregated to HyspIRI-scale (60-m) pixels. As shown in these temperature maps, the aggregation of radiance resulted in a decrease of  $\sim 60\text{ K}$  in the maximum observed temperature: 1101 vs. 1043 K.

Figure 22 depicts ASTER data acquired over Kilauea Volcano, Hawaii, on November 25, 2007, during an outbreak of surface activity. These data were acquired during a nighttime overpass to eliminate the contributions of reflected solar irradiance to the temperature estimates. The active flow field is prominent Figure 22(a), an example of ASTER TIR data. The high temperatures of the active flows resulted in saturation of the TIR and SWIR data. The twin panels below the TIR scene are temperature maps derived from Channel 3 radiance. Figure 22(b) shows the temperatures derived from radiance at the native spatial resolution, and Figure 22(c) shows the temperatures derived from Channel 3 radiance aggregated to HyspIRI-scale pixels. The aggregation resulted in a decrease of  $\sim 130\text{ K}$  in the maximum observed temperature: 1122 vs. 993 K. This large reduction in maximum temperature, relative to the aggregation-based reduction in the maximum temperature of the Klyuchevskoy flow (Figs. 21[b] and 21[c]), is a consequence of the smaller size and isolated nature of the Kilauea hot spots (Figs. 22[b] and 22[c]).

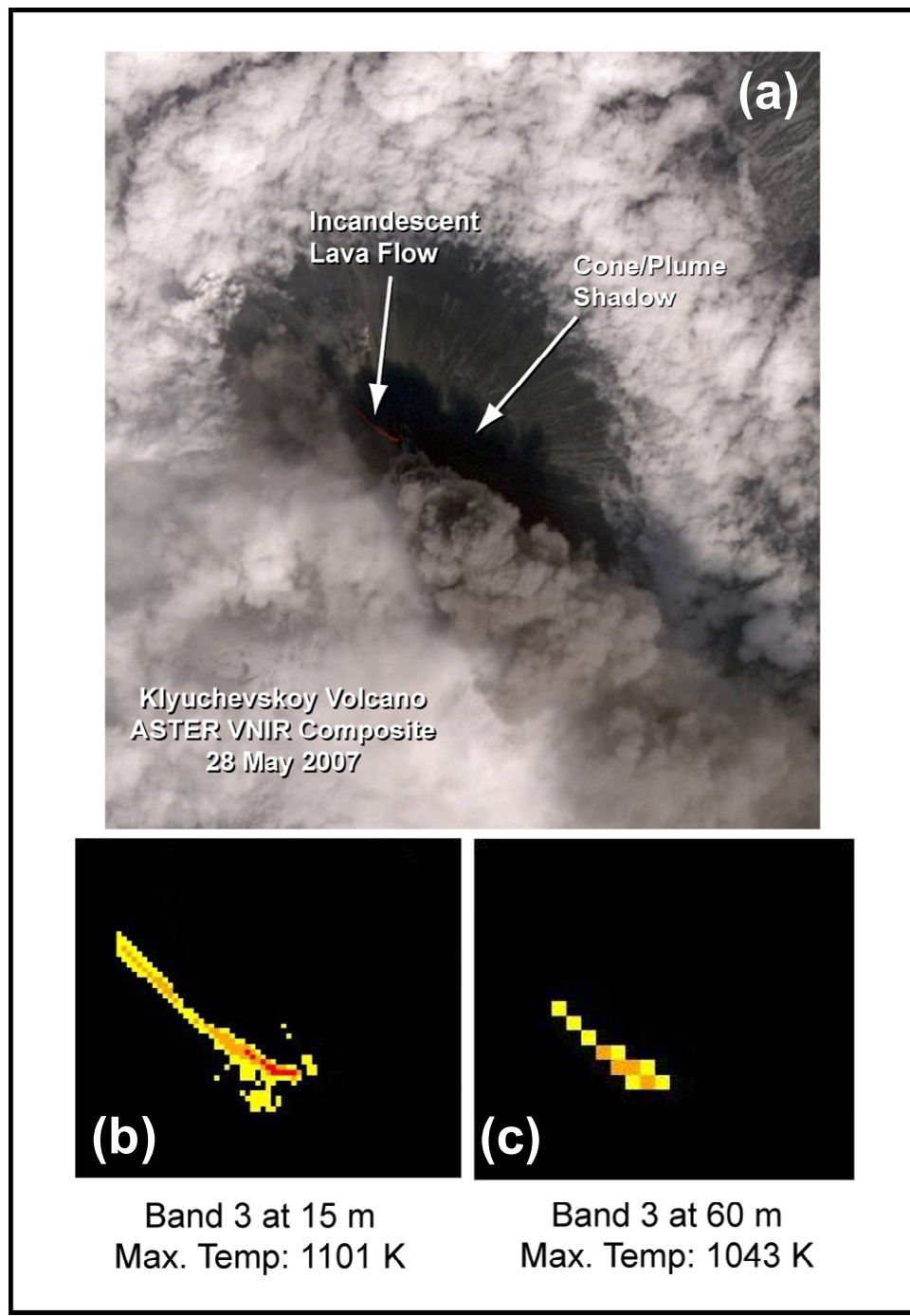


**Figure 21. ASTER data acquired over Klyuchevskoy Volcano.**  
(a) Color-composite of ASTER VNIR data showing incandescent lava flow in the shadow cast by an eruption plume; (b) lava flow temperatures derived from Channel 3 (0.807  $\mu\text{m}$ ) radiance measurements; (c) lava flow temperatures derived from Channel 3 radiance following aggregation to 60-m pixels [data courtesy of M. Ramsey].

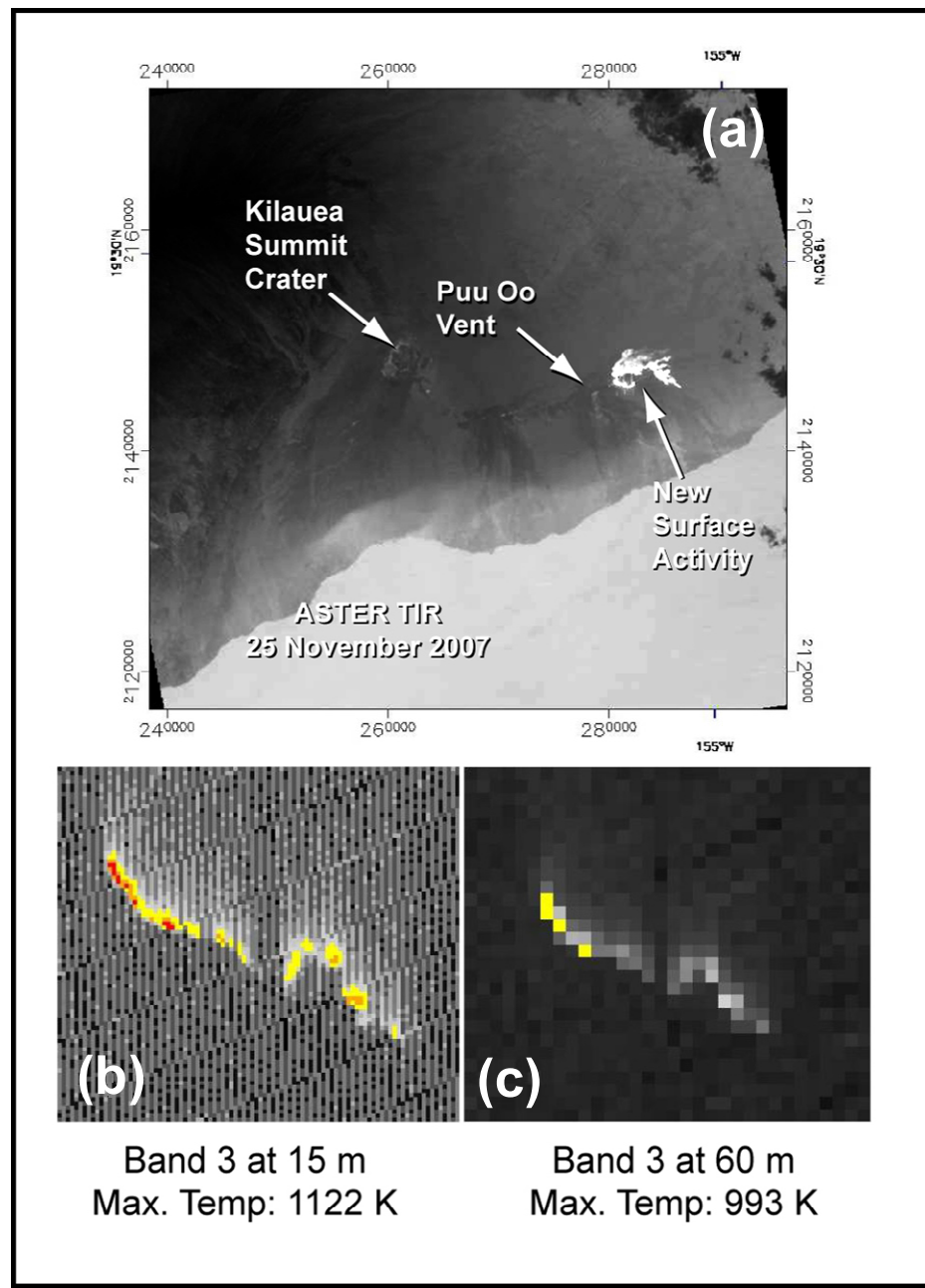


**Figure 22. ASTER data acquired over Kilauea Volcano, Hawaii.**  
 (a) Night-time TIR data, showing active lava flow field; (b) lava flow temperatures derived from Channel 3 (0.807  $\mu\text{m}$ ) radiance measurements; (c) temperatures derived from Channel 3 radiance following aggregation to 60-m pixels [data courtesy of M. Ramsey].

#### 4.2.5 *Hyperion Surveys of Nyamuragira and Eyjafjallajökull Volcanoes*

Figures 23 and 24 feature 4- $\mu\text{m}$  temperature maps for Nyamuragira (DR-Congo) and Eyjafjallajökull (Iceland) Volcanoes as simulated from hyperspectral V-SWIR radiance spectra measured with Hyperion. The Hyperion data were acquired at night to eliminate the contributions of reflected solar irradiance to the temperature estimates. At the time the Nyamuragira data were acquired, May 21, 2004, the activity at the volcano was near the end of an eruption episode that began on May 8, 2004 and ended sometime between May 25 and 31, 2004. The Eyjafjallajökull data were acquired on April 1, 2010, during an eruption that began with the opening of a fissure on March 20, 2010. The data acquisition coincided with the opening of a new fissure on March 31, and the data depict lava fountains from both fissures.

The temperature maps (Figs. 23 and 24) are the results of a multi-step analysis procedure. For each pixel in the Hyperion data, we derived sub-pixel temperature components and corresponding area fractions through an application of the minimized multi-component procedure (see Figure 10). The resulting temperature distribution was used to calculate a continuous (VIS through TIR) radiance spectrum, which we convolved with the notional spectral response of the HyspIRI 4- $\mu\text{m}$  channel to simulate radiance measured in this channel. Figures 23(a) and 24(a) are maps of the temperatures derived from this simulated radiance at the native (30-m) spatial resolution of Hyperion. Figures 23(b) and 24(b) are maps of temperatures derived from radiance aggregated to HyspIRI-scale pixels. The aggregation resulted in a reductions of approximately 150 and 350 K in the maximum temperatures for the Nyamuragira flow field (1100 vs. 950 K) and Eyjafjallajökull fissures (1100 vs. 750 K), respectively.

The bottom set of panels indicate the pixels that would be saturated with 4- $\mu\text{m}$  saturation temperature settings of 800–1000 K (Figs. 23[c], [d], and [e]) in the case of Nyamuragira and 700–900 K in the case of Eyjafjallajökull (Figs. 24[c], [d], and [e]). We see that saturation temperature settings of 1000 and 900 K, respectively, would be required to prevent saturation of HyspIRI data acquired during Nyamuragira- and Eyjafjallajökull-class eruptions.

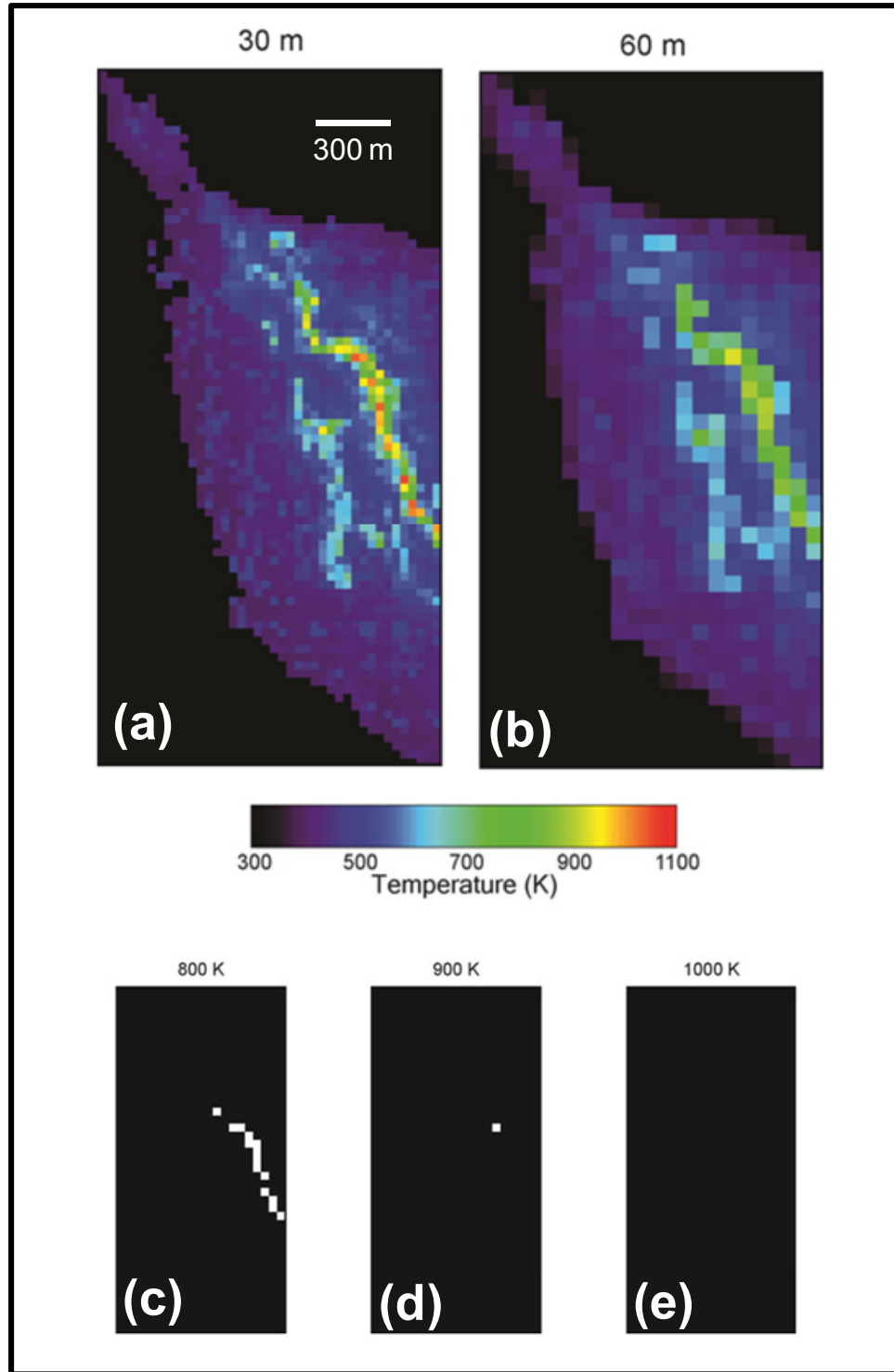


**Figure 23.** Analysis of Hyperion data acquired over Nyamuragira Volcano on 21 May 2004. (a) Simulated 4- $\mu$ m temperatures at native (30 m) spatial resolution of Hyperion; (b) simulated 4- $\mu$ m temperatures for aggregated, HyspIRI-scale pixels; (c) – (e) maps of pixels saturated for saturation temperature settings of 800, 900, and 1000 K, respectively [data courtesy of R. Wright].

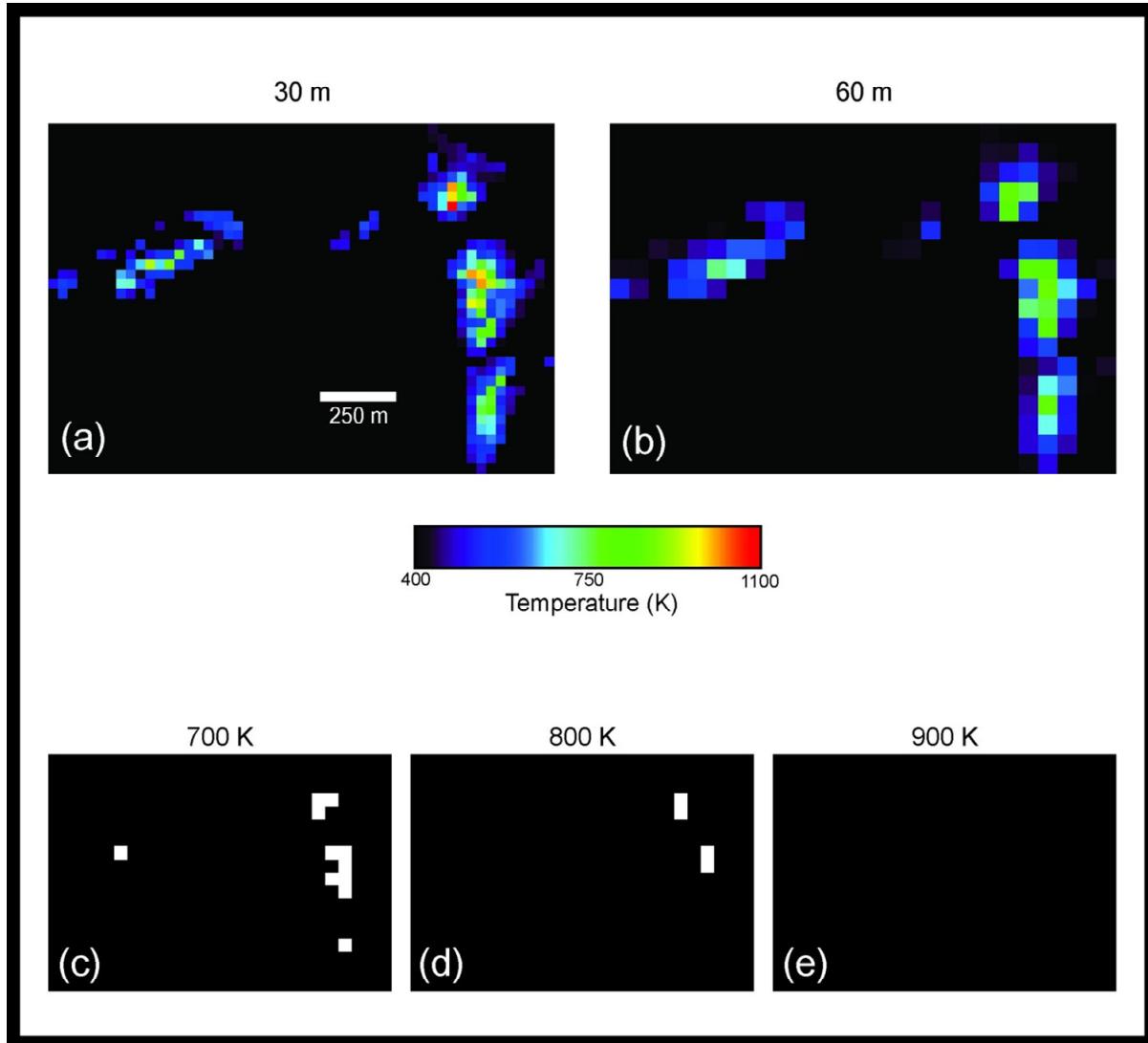


**Figure 24.** Analysis of Hyperion data acquired over Eyjafjallajökull Volcano on 1 April 2010. (a) Simulated 4-mm temperatures at native (30 m) spatial resolution of Hyperion; (b) simulated 4-mm temperatures for aggregated, HyspIRI-scale pixels; (c) – (e) maps of pixels saturated for saturation temperature settings of 700, 800, and 900 K, respectively [data courtesy of R. Wright].

## 5 Conclusion

Table 4 summarizes the results of our case studies, together with the highest temperature estimates published for the Lake Baikal Fire of 2003 (Zhukov et al. 2006) and Krafla eruption of 1984 (Harris et al. 1995a). Based on these results we recommend a 4- $\mu\text{m}$  saturation temperature setting of 1200 K. This setting will prevent saturation for all of the temperatures found in our studies with the exception of the Sharpsand Fire (and we note that the lower of our simulated HyspIRI temperatures for this fire was 1205 K) and the Krafla Eruption of 1984.

Referring to Figure 2, a saturation temperature of 1200 K will result in NE $\Delta$ T levels of 8–4.5 K for scene temperatures in the range 320–340 K, respectively. The proposed NE $\Delta$ T levels are too high for land- and sea-surface temperature studies with the HyspIRI 4- $\mu\text{m}$  channel, but the TIR channels between 8 and 12  $\mu\text{m}$  (Fig. 1) will be well-suited for studies of ambient surface temperatures. In addition, we note that HyspIRI data acquired over the oceans will be aggregated into 960-m pixels (representing a 16 x 16 block of 60-m pixels) with a corresponding 16 times improvement in NE $\Delta$ T. The aggregated 4- $\mu\text{m}$  radiance data may fit the needs of the sea-surface temperature community.

The trade-off between saturation temperature and sensitivity is particularly acute for fire and hotspot detection techniques, and the full impact of the proposed NE $\Delta$ T on such algorithms has yet to be determined. For example, the Fire Radiant Power (FRP) algorithm will require us to measure fire temperatures together with temperatures adjacent to the active fire fronts. A smoldering fire at 700 K occupying 1% (36  $\text{m}^2$ ) of a HyspIRI pixel at an ambient temperature of 320 K would increase the 4- $\mu\text{m}$  temperature to  $\sim$ 380 K. Given an NE $\Delta$ T of 8 K, we could calculate the FRP of this modest fire with an uncertainty of  $\pm$  6%. An increase in the 4- $\mu\text{m}$  saturation temperature setting from 1200 to 1300 K would increase the NE $\Delta$ T by 25% (10 K vs. 8 K), with a corresponding increase in uncertainty for the FRP estimation.

The trade-off between saturation at scene temperatures  $>$  1200 K, as encountered during the Krafla eruption, and increased sensitivity to smoldering ( $\sim$ 700 K) fires is acceptable, given the high probability of observing such fires over the life of a HyspIRI mission relative to the probability of observing another Krafla-scale eruption. With regard to volcanic phenomena, we note that the proposed saturation temperature of 1200 K is higher than the Klyuchevskoy (Fig. 21[b]), Kilauea (Fig. 22[b]), Nyamuragira (Fig. 23[a]), or Eyjafjallajökull (Fig. 24[a]) temperatures estimated at the native spatial resolution of ASTER or Hyperion.

**Table 4. Summary of Maximum Temperatures from Team and Published Studies**

Case Study	Instrument	Maximum Temperature
Sharpsand Fire, 2007	AGEMA Thermal Camera	1205/1260 K
Klyuchevskoy Volcano, 2007	ASTER VNIR	1043 K
Kilauea Volcano, 2007	ASTER VNIR	990 K
Nyamuragira Volcano, 2004	Hyperion SWIR	950 K
Indians Fire, 2008	AVIRIS SWIR	860 K
Poomacha Fire, 2007	AMS TIR	795 K
Published Study	Instrument	Maximum Temperature
Krafla Eruption, 1984 (Harris et al. 1995)	AVHRR MIR	1325 K
Lake Baikal Fire, 2003 (Zhukov et al. 2006)	HSRS MIR	988 K

## 6 Selected Bibliography

---

Boschetti, L., and D. P. Roy (2009), Strategies for the fusion of satellite fire radiative power with burned area data for fire radiative energy derivation, *J. Geophys. Res.*, 114, D20302, doi:10.1029/2008JD011645

Briess, K., H. Jahn, E. Lorenz, D. Oertel, W. Skrbek, and B. Zhukov (2003), Fire recognition potential of the bi-spectral Infrared detection (BIRD) satellite, *Int. J. Remote Sens.*, 24(4), 865-872.

Carter, A.J., O. Girina, M.S. Ramsey, and Y.V. Demyanchuk (2008), ASTER and field observations of the 24 December 2006 eruption of Bezymianny Volcano, Russia, *Remote Sens. Environ.*, 112, 2569-2577.

Carter, A.J., and M.S. Ramsey (2009), ASTER- and field-based observations at Bezymianny Volcano: focus on the 11 May 2007 pyroclastic flow deposit, *Remote Sens. Environ.*, 113, 2142-2151.

Csiszar, I., and J. Sullivan (2002), Recalculated pre-launch saturation temperatures of the AVHRR 3.7  $\mu$ m sensors on board the TIROS-N to NOAA-14 satellites, *Int. J. Remote Sens.*, 23(24), 5271-5276.

Csiszar, I.A., J.T. Morisette, and L. Giglio (2006), Validation of active fire detection from moderate-resolution satellite sensors: the MODIS example in northern Eurasia, *IEEE Trans. Geosci. Remote Sens.*, 44(7), 1757-1764, doi: 10.1109/TGRS.2006.875941.

Dennison, P.E., K. Charoensiri, D.A. Roberts, S.H. Peterson, and R.O. Green (2006), Wildfire temperature and land cover modeling using hyperspectral data, *Remote Sens. Environ.*, 100(2), 212-222.

Dennison, P.E., and D.S. Matheson (2011), Comparison of fire temperature and fractional area modeled from SWIR, MIR, and TIR multispectral and SWIR hyperspectral airborne data, *Remote Sens. Environ.*, 115(3), 876-886.

Dozier, J. (1981), A method for satellite identification of surface temperature fields of subpixel resolution, *Remote Sens. Environ.*, 11, 221-229.

Earth Science and Applications from Space: National Imperatives for the Next Decade and Beyond, 2007. Committee on Earth Science and Applications from Space: A Community Assessment and Strategy for the Future (2007). National Research Council, National Academies Press. Referred to as the Decadal Survey or NRC 2007.

Eckmann, T.C., D.A. Roberts, and C.J. Still (2008), Using multiple endmember spectral mixture analysis to retrieve subpixel fire properties from MODIS, *Remote Sens. Environ.*, 112, 3773-3783.

Eckmann, T.C., D.A. Roberts, and C.J. Still (2009) Estimating subpixel fire sizes and temperatures from ASTER using multiple endmember spectral analysis, *Int. J. Remote Sens.*, 30(22), 5851-5864.

Ellicott, E., E. Vermote, L. Giglio, and G. Roberts, Estimating biomass consumed from fire using MODIS FRE (2009), *Geophys. Res. Lett.*, 36, L13401, doi:10.1029/2009GL038581.

Freeborn, P.H., M.J. Wooster, W.M. Hao, C.A. Ryan, B.L. Nordgren, S.P. Baker, and C. Ichoku (2008), Relationships between energy release, fuel mass loss, and trace gas and aerosol emissions during laboratory biomass fires, *J. Geophys. Res.*, 113, D01301, doi:10.1029/2007JD008679.

Gao, B-C, X. Xiong, R-R Li, and D-Y Wang (2007), Evaluation of the Moderate Resolution Imaging Spectrometer special 3.95-mm fire channel and implications on fire channel selections for future satellite instruments, *J. Appl. Remote Sens.*, 1, 013516, doi: 10.1117/1.2757715.

Giglio, L., J.D. Kendall, and C.O. Justice (1999), Evaluation of global fire detection algorithms using simulated AVHRR infrared data, *Int. J. Remote Sens.*, 20(10), 1947-1985.

Giglio, L., J.D. Kendall, and C.J. Tucker (2000), Remote sensing of fires with the TRMM VIRS, *Int. J. Remote Sens.*, 21(1), 203-207.

Giglio, L. and J. D. Kendall (2001), Application of the Dozier retrieval to wildfire characterization - a sensitivity analysis, *Remote Sens. Environ.*, 77, 34-49.

Giglio, L., J. Descloitres, C.O. Justice, and Y.J. Kaufman (2003), An enhanced contextual fire detection algorithm for MODIS, *Remote Sens. Environ.*, 87, 273-282, doi:10.1016/S0034-4257(03)00184-6.

Giglio, L. and C.O. Justice (2003), Effects of wavelength selection on characterization of fire size and temperature, *Int. J. Remote Sens.*, 24(17), 3515-3520, doi:10.1080/0143116031000117056.

Giglio, L., J.D. Kendall, and R. Mack (2003), A multi-year active fire dataset for the tropics derived from the TRMM VIRS, *Int. J. Remote Sens.*, 24(22), 4505-4525.

Giglio, L., I. Csizsar, A. Restas, J.T. Morisette, W. Schroeder, D. Morton, and C.O. Justice (2008), Active fire detection and characterization with the advanced spaceborne thermal emission and reflection radiometer (ASTER), *Remote Sens. Environ.*, 112, 3055-3063, doi:10.1016/j.rse.2008.03.003.

Giglio, L., T. Loboda, D.P. Roy, B. Quayle, and C.O. Justice (2009), An active-fire based burned area mapping algorithm for the MODIS sensor, *Remote Sens. Environ.*, 113, 408-420, doi:10.1016/j.rse.2008.10.006.

Harris, A.J.L., and C.R. Thornber (1999), Complex effusive events at Kilauea as documented by the GOES satellite and remote video cameras, *Bull. Volcanol.*, 61, 382-395.

Harris, A.J.L., L.P. Flynn, D.A. Rothery, C. Oppenheimer, and S.B. Sherman (1999), Mass flux measurements at active lava lakes, *J. Geophys. Res.*, 104(B4), 7117-7136.

Harris, AJL, R.A. Vaughan, and D.A. Rothery (1995a), Volcano detection and monitoring using AVHRR data: the Krafla eruption, 1984, *Int. J. Remote Sens.*, 16(6), 1001-1020.

Harris, A.J.L. , D.A. Rothery, R.W. Carlton, S. Langaas, and H. Mannstein (1995b), Non-zero saturation of AVHRR thermal channels over high temperature targets: evidence from volcano data and a possible explanation, *Int. J. Remote Sens.*, 16(1), 189 -196.

Harris, A.J.L., S. E. J. Swabey, and J. Higgins (1995c), Automated thresholding of active lavas using AVHRR data, *Int. J. Remote Sens.*, 16, 3681-3686.

Harris, A. J. L., L. Keszthelyi, L. P. Flynn, P. J. Mouginis-Mark, C. Thornber, J. Kauahikaua, D. Sherrod, F. Trusdell, M. W. Sawyer, and P. Flament (1997a), Chronology of the episode 54 eruption at Kilauea volcano, Hawaii, from GOES-9 satellite data, *Geophys. Res. Lett.*, 24, 3281–3284.

Harris, A.J.L., S. Blake, D. A. Rothery, and N.F. Stevens (1997b), A chronology of the 1991 to 1993 Etna eruption using advanced very high resolution radiometer data: Implications for real-time thermal volcano monitoring, *J. Geophys. Res.*, 102, 7985–8003.

Harris, A. J. L., et al., Real-time monitoring of volcanic hot spots with satellites, in *Remote Sensing of Active Volcanism*, *Geophys. Monogr. Ser.*, vol. 116, edited by P. J. Mouginis-Mark, J. A. Crisp, and J. H. Fink, pp. 139–159, AGU, Washington, D. C., 2000.

Harris, A. J. L., E. Pilger, L. P. Flynn, H. Garbeil, P. J. Mouginis-Mark, J. Kauahikaua, and C. Thornber (2001), Automated, high temporal resolution, thermal analysis of Kilauea volcano, Hawai'i, using GOES satellite data, *Int. J. Remote Sens.*, 22, 945–967.

Justice, C.O., L. Giglio, S. Korontzi, J. Owens, J.T. Morisette, D. Roy, J. Descloitres, S. Alleaume, F. Petitcolin, and Y. Kaufman (2002), The MODIS fire products, *Remote Sens. Env.*, 83, 244 – 262.

Kaufman, Y.J., R.G. Kleidman, and M.D. King (1998a), SCAR-B fires in the tropics: properties and remote sensing from EOS-MODIS, *J. Geophys. Res.*, 103(D24), 31,955-31,968.

Kaufman, Y.J., C.O. Justice, L.P. Flynn, J.D. Kendall, E.M. Prins, L. Giglio, D.E. Wards, W.P. Menzel, and A.W. Setzer (1998b), Potential global fire monitoring from EOS-MODIS, *J. Geophys. Res.*, 103(D24), 32,215-32,238.

Kaufman, Y.J., C. Ichoku, L. Giglio, S. Korontzi, D.A. Chu, W.M. Hao, R.R. Li, and C. Justice (2003), Fire and smoke observed from Earth Observing System MODIS instrument – products, validation, and operational use, *Int. J. Remote Sens.*, 24(8), 1765-1781.

Langaas, S. (1993) A parameterised bispectral model for savanna fire detection using AVHRR night images, *Int. J. Remote Sens.*, 14(12), 2245-2262.

Lombardo, V., M.F. Buongiorno, and S. Amici (2006), Characterization of volcanic thermal anomalies by means of sub-pixel temperature distribution analysis, *Bull. Volcanol.*, 68, 641-651.

Matson, M., and J. Dozier (1981), Identification of subresolution high temperature sources using a thermal IR sensor, *Photogram. Eng. Remote Sens.*, 47(9), 1311-1318.

Morisette, J.T., L. Giglio, I. Csiszar, and C.O. Justice (2005a), Validation of the MODIS active fire product over Southern Africa with ASTER data, *Int. J. Remote Sens.*, 26(10), 4239-4264.

Morisette, J.T., L. Giglio, I. Csiszar, A. Setzer, W. Schroeder, D. Morton, and C.O. Justice (2005b), Validation of MODIS active fire detection products derived from two algorithms, *Earth Interact.*, 9(9), 1-25.

Oertel, D., B. Zhulov, H-P Thamm, J. Roehrig, and B. Orthmann (2004) Space-borne high resolution fire remote sensing in Benin, West Africa, *Int. J. Remote Sens.*, 25(11), 2209-2216.

Oppenheimer, C., P.W. Francis, D.A. Rothery, and R.W.T. Carlton (1993a), Infrared Image Analysis of Volcanic Thermal Features: Lascar Volcano, Chile, 1984-1992, *J. Geophys. Res.*, *98(B3)*, 4269-4286.

Oppenheimer, C., D.A. Rothery, D.C. Pieri, D.C. Pieri, M.J. Abrams, and V. Carrere (1993b), Analysis of Airborne Visible/Infrared Imaging Spectrometer data of volcanic hot spots, *Int. J. Remote Sens.*, *14(16)*, 2919-2934.

Pereira, G., S.R. Freitas, E.C. Moraes, N.J. Ferreira, Y.E. Shiombukuro, V.B. Rao, and K.M. Longo (2009), Estimating trace gas and aerosol emissions over South America: relationship between fire radiative energy released and aerosol optical depth observations, *Atmos. Environ.*, *43*, 6388-6391.

Ramsey, M., and J. Dehn (2004), Spaceborne observations of the 2000 Bezymianny, Kamchatka eruption: the integration of high-resolution ASTER data into near real-time monitoring using AVHRR, *J. Volcanol. Geotherm. Res.*, *135*, 127-146.

Riggan, P.J., J.A. Brass, and R.N. Lockwood (1993), Assessing fire emissions from tropical savanna and forest of central Brazil, *Photogram. Eng. Remote Sens.*, *59(6)*, 1009-1015.

Riggan, P.J., R.G. Tissell, R.N. Lockwood, J.A. Brass, J.A.R. Pereira, H.S. Miranda, A.C. Miranda, T. Campos, and R. Higgans (2004), *Ecolog. Appl.*, *14(3)*, 855-872.

Roberts, D.A., M. Gardner, R. Church, S. Ustin, G. Scheer, and R.O. Green (1998), Mapping chaparral in the Santa Monica Mountains using multiple endmember spectral mixture models, *Remote Sens. Environ.*, *65*, 267-279.

Roberts, G., M. J. Wooster, G. L. W. Perry, N. Drake, L.-M. Rebelo, and F. Dipotso (2005), Retrieval of biomass combustion rates and totals from fire radiative power observations: Application to southern Africa using geostationary SEVIRI imagery, *J. Geophys. Res.*, *110*, D21111, doi:10.1029/2005JD006018.

Roberts, G.J., and M.J. Wooster (2008) Fire detection and fire characterization over Africa using Meteosat SEVIRI, *IEEE Trans. Geosci. Remote Sens.*, *46(4)*, 1200-1218.

Rose, S., and M. Ramsey (2009) The 2005 eruptin of Kliuchevskoi volcano: chronology and processes derived from ASTER spaceborne and field-based data, *J. Volcanol. Geotherm. Res.*, *184*, 367-380.

Siegert, F., B. Zhukov, D. Oertel, S. Limin, S.E. Page, J.O. Rieley (2004) Peat fires detected by the BIRD satellite, *Int. J. Remote Sens.*, *25(16)*, 3221-3230.

Smith, D.R., J.D. Kaduk, et al., (2010), Soil surface CO<sub>2</sub> flux increases with successional time in a fire scar chronosequence of Canadian boreal jack pine forest, *Biogeosci.*, *7*, 1375-1381, doi:10.5194/bg-7-1375-2010.

Vaughan, R.G., M. Kervyn, V. Realmuto, M. Abrams, and S.J. Hook (2008), Satellite measurements of recent volcanic activity at Oldoinyo Lengai, Tanzania, *J. Volcanol. Geotherm. Res.*, *173*, 196-206.

Wooster, M. J., and D. A. Rothery (1997), Thermal monitoring of Lascar Volcano, Chile, using infrared data from the along-track scanning radiometer: a 1992-1995 time series, *Bull. Volcanol.*, *58*, 566-579.

Wooster, M.J., T. Kaneko, S. Nakada, and H. Shimizu (2000), Discrimination of lava dome activity styles using satellite-derived thermal structures, *J. Volcanol. Geotherm. Res.*, *102*, 97-118.

Wooster, M.J., and T. Kaneko (2001), Testing the accuracy of solar-reflected radiation corrections applied during satellite shortwave infrared thermal analysis of active volcanoes, *J. Geophys. Res.*, *106(B7)*, 13,381-13,393.

Wooster, M.J., B. Zhukov, and D. Oertel (2003), Fire radiative energy for quantitative study of biomass burning: derivation from the BIRD experimental satellite and comparison to MODIS fire products, *Remote Sens. Environ.*, *86*, 83-107, doi:10.1016/S0034-4257(03)00070-1.

Wooster, M.J., G. Roberts, G.L.W. Perry, and Y.J. Kaufman (2005), Retrieval of biomass combustion rates and totals from fire radiant power observations: FRP derivation and calibration relationship between biomass consumption and fire radiative energy release, *J. Geophys. Res.*, *110*, D24311, doi:10.1029/2005JD006318.

Wright, R., L.P. Flynn, and A.J.L. Harris (2001), Evolution of lava flow-fields at Mount Etna, 27-28 October 1999, observed by Landsat ETM+, *Bull. Volcanol.*, *63*, 1-7.

Wright, R., L. P. Flynn, H. Garbeil, A. J. S. Harris, and E. Pilger (2002), Automated volcanic eruption detection using MODIS, *Remote Sens. Environ.*, *82*, 135–155

Wright, R., and L.P. Flynn (2003), On the retrieval of lava-flow surface temperatures from infrared satellite data, *Geology*, *31*, 893-896, doi:10.1130/G19645.1

Wright, R., L.P. Flynn, H. Garbeil, A. J. L. Harris, and E. Pilger (2004), MODVOLC: near-real-time thermal monitoring of global volcanism, *J. Volcanol. Geothermal Res.*, *135*, 29–49

Wright, R., H. Garbeil, and A.G. Davies (2010), Cooling rate of some active lavas determined using an orbital imaging spectrometer, *J. Geophys. Res.*, *115*, B06205, doi:10.1029/2009JB006536

Xiong, X., B.N. Wenny, A. Wu, W.L. Barnes, and V.V. Salmonson (2009), Aqua MODIS thermal emissive band on-orbit calibration, characterization, and performance, *IEEE Trans. Geosci. Remote Sens.*, *47(3)*, 803-814, doi: 10.1109/TGRS.2008.2005109

Xu, W., M.J. Wooster, G. Roberts, and P. Freeborn (2010), New GOES imager algorithms for cloud and active fire detection and fire radiative power assessment across North, South, and Central America, *Remote Sens. Env.*, *114*, 1876-1895.

Zhukov, B., K. Briess, E. Lorenz, D. Oertel, and W. Skrbek (2005), Detection and analysis of high-temperature events in the BIRD mission, *Acta Astro.*, *56*, 65-71.

Zhukov, B., E. Lorenz, D. Oertel, M. Wooster, and G. Roberts (2006), Spaceborne detection and characterization of fires during the bi-spectral infrared detection (BIRD) experimental small satellite mission (2001-2004), *Remote Sens. Environ.*, *100*, 29-51.

---

REPORT DOCUMENTATION PAGE					Form Approved OMB No. 0704-0188
<p>The public reporting burden for this collection of information is estimated to average 1 hour per response, including the time for reviewing instructions, searching existing data sources, gathering and maintaining the data needed, and completing and reviewing the collection of information. Send comments regarding this burden estimate or any other aspect of this collection of information, including suggestions for reducing this burden, to Department of Defense, Washington Headquarters Services, Directorate for Information Operations and Reports (0704-0188), 1215 Jefferson Davis Highway, Suite 1204, Arlington, VA 22202-4302. Respondents should be aware that notwithstanding any other provision of law, no person shall be subject to any penalty for failing to comply with a collection of information if it does not display a currently valid OMB control number.</p>					
<b>PLEASE DO NOT RETURN YOUR FORM TO THE ABOVE ADDRESS.</b>					
1. REPORT DATE (DD-MM-YYYY) 00-04-2011		2. REPORT TYPE JPL Publication			3. DATES COVERED (From - To) N/A
4. TITLE AND SUBTITLE HyspIRI High-Temperature Saturation Study			5a. CONTRACT NUMBER NAS7-03001		
			5b. GRANT NUMBER		
			5c. PROGRAM ELEMENT NUMBER		
6. AUTHOR(S) V. Realmuto, S. Hook, M. Foote, G. Vaughan, I. Csiszar, P. Dennison, L. Giglio, M. Ramsey, M. Wooster, R. Wright			5d. PROJECT NUMBER 103932		
			5e. TASK NUMBER H08.1		
			5f. WORK UNIT NUMBER		
7. PERFORMING ORGANIZATION NAME(S) AND ADDRESS(ES) Jet Propulsion Laboratory California Institute of Technology 4800 Oak Grove Drive Pasadena, CA 91009			8. PERFORMING ORGANIZATION REPORT NUMBER JPL Publication 11-2		
9. SPONSORING/MONITORING AGENCY NAME(S) AND ADDRESS(ES) National Aeronautics and Space Administration Washington, DC 20546-0001			10. SPONSORING/MONITOR'S ACRONYM(S) NASA/NOAA/USGS/NRC		
			11. SPONSORING/MONITORING REPORT NUMBER		
12. DISTRIBUTION/AVAILABILITY STATEMENT Unclassified—Unlimited Subject Category 46 Geophysics Availability: NASA CASI (301) 621-0390      Distribution: Nonstandard					
13. SUPPLEMENTARY NOTES					
14. ABSTRACT As part of the precursor activities for the HyspIRI mission, a small team was assembled to determine the optimum saturation level for the mid-infrared (4-μm) channel, which is dedicated to the measurement of hot targets. Examples of hot targets include wildland fires and active lava flows. This determination took into account both the temperature expected for the natural phenomena and the expected performance of the mid-infrared channel as well as its overlap with the other channels in the thermal infrared (7.5–12 μm) designed to measure the temperature of lower temperature targets. Based on this work, the hot target saturation group recommends a saturation temperature of 1200 K for the mid-infrared channel. The saturation temperature of 1200 K represents a good compromise between the prevention of saturation and sensitivity to ambient temperature.					
15. SUBJECT TERMS saturation, imaging spectrometer, infrared spectrometer, Earth movements					
16. SECURITY CLASSIFICATION OF: a. REPORT U b. ABSTRACT U c. THIS PAGE U			17. LIMITATION OF ABSTRACT UU	18. NUMBER OF PAGES 52	19a. NAME OF RESPONSIBLE PERSON STI Help Desk at help@sti.nasa.gov 19b. TELEPHONE NUMBER (Include area code) (301) 621-0390